Coastal Engineering 168 (2021) 103893

Contents lists available at ScienceDirect

Coastal Engineering

journal homepage: www.elsevier.com/locate/coastaleng

# Breaking bore roller characteristics: Turbulence statistics using optical techniques

Rui Shi [a,*], Xinqian Leng [a,b], Hubert Chanson [a]

[a] The University of Queensland, School of Civil Engineering, Brisbane, QLD, 4072, Australia
[b] University of Bordeaux, I2M, Laboratoire TREFLE, Pessac Cedex, France

ARTICLE INFO

*Keywords:*
Aeration
Air-water flow properties
Breaking bore
Optical flow
Roller toe
Turbulence
Physical modelling

ABSTRACT

Surface wave breaking induces strong turbulence in the two-phase flow region. Detailed turbulence statistics were experimentally obtained using non-intrusive optical techniques in a breaking bore roller, at relatively large scale, with a bore Froude number $Fr_1 = 2.15$ and Reynolds number $\mathrm{Re} = 2.3 \times 10^5$. These novel velocity data were ensemble-averaged based upon an instantaneous dataset of 24,320 images. In terms of the velocity field, the breaking bore roller was classified into three regions: the impinging jet, developing shear layer and flow reversal region. The vertical profiles of the longitudinal velocity data exhibited some self-similarity. The Reynolds stress data showed an anisotropic turbulent flow immediately downstream of the roller toe, and tended towards isotropy away from the roller toe. The vorticity data suggested that the breaking at the roller toe was responsible for the generation of vortices. The turbulent structures in the shear layer presented significantly smaller length and time scales with higher dissipation rate than other regions. A discussion between present turbulence statistical data and bubble dynamics from literature was developed. The comparison between present and past studies suggested a similarity in two-phase physical processes in the breaking roller region between the tidal bore, hydraulic jump, swash zone bore and breaking wave.

## 1. Introduction

Bores are seen from a variety of free-surface flows (Fig. 1), such as tidal bores occurring in river estuary (Chanson, 2011), bores evolved from breaking waves and swash flows, tsunami bores (Yeh, 1991), and dam-break flows (Dressler, 1954). The last two flows often propagate on both dry and wet beds, leading to different flow characteristics (Wüthrich et al., 2018). The present study only covers the bores on wet beds in a rectangular channel, and the bore strength is characterised by the bore Froude number (Rayleigh, 1908):

$$Fr_1 = \frac{V_1 + U}{\sqrt{g d_1}} \tag{1}$$

where $d_1$ is the flow depth of initial steady flow, g is the gravity constant, $U$ is the mean bore celerity and $V_1$ is the cross-sectional averaged velocity of the initial steady flow.

Apart from the unique generation conditions, the difference between above bores propagating on the wet bed is the resistance of the bottom boundary (Madsen and Svendsen, 1983). In a tidal bore, the resistance of the bottom boundary is induced by the opposite travel direction between the bore propagation and initial steady current. A strong initial current could hold the bore stationary, which became a hydraulic jump (Peregrine, 1983). A bore propagating on quiescent water (e.g. spilling waves) has a weaker resistance of bottom boundary.

On the other hand, the bores formed from above scenarios exhibit similar physical processes. Based on the bore Froude number, the bores can be undular ($Fr_1 < 1.3$–$1.4$) and breaking ($Fr_1 > 1.4$) (Leng and Chanson, 2016). The undular bores are featured with a smooth wave front followed with a train of secondary undulations, and the theoretical considerations were given in the classic works of Peregrine (1966) and Soares Frazao and Zech (2002). The similarities of the breaking bores are shown in terms of free-surface properties, air entrainment process and flow characteristics. A common feature on these free surfaces is the flow discontinuity at the bore front, where at its downstream, strong turbulence significantly distorts the free surfaces, generating splash and droplets (Brocchini and Peregrine, 2001). The strong free-surface turbulence results into air-water exchange, together with the air entrainment by secondary plunging surface waves and air extrusion over the bore front, being the basic air entrainment mechanisms (Kiger and

* Corresponding author.
*E-mail address:* rui.shi@uq.net.au (R. Shi).

https://doi.org/10.1016/j.coastaleng.2021.103893
Received 28 April 2020; Received in revised form 28 November 2020; Accepted 27 March 2021
Available online 3 April 2021
0378-3839/

Duncan, 2012). The similar physical processes are observed from the flow regions and turbulence. The most featured part of the breaking bores is the breaking "roller", in which the water recirculates down the bore front, advecting the entrained air bubbles (Peregrine, 1983). Large-scale vortices generate immediately downstream of the bore front because of the Kelvin-Helmholtz type of instability (Lubin et al., 2019). The advection of these vortices in the shear zone initially behave as two-dimensional structures, while away from the roller, strong three-dimensionality is developed (Nadaoka et al., 1989).

While many works revealed great details on the flow characteristics underneath the breaking rollers (Hornung et al., 1995; Melville et al., 2002; Leng and Chanson, 2019a), little has been undertaken experimentally in the breaking roller, because of the difficulty to implement the traditional instrumentation (ADV, LDV and PIV). Yeh and Mok (1990) generated breaking bores using a dam-break way, showing that the bore roller takes "generation and advection" cycles induced by the large-scale recirculating vortices. The evolutions of these vortices were observed by Nadaoka et al. (1989), who also suggested that the advection of the large-scale vortices generated new source of vorticity. Cowen et al. (2003) was able to use PIV in slightly aerated wash zone flows by fluorescent particle/filter combination, showing that the uprush phase acted as a turbulent bore. Huang et al. (2009) presented the global distributions of turbulence dissipation rate in a swash zone, where a spilling breaker developed to a breaking bore. Since the breaking bore exhibited slight aeration, and they were able to provide the data near the bore front, showing that the large-scale vortices dominated the dynamics of turbulent dissipation in the surf zone. Wüthrich et al. (2020a) investigated the transverse periodicity of the bore front, owing to the large-scale transverse coherent structures in the breaking roller. Wüthrich et al. (2020b) classified the most reoccurring air-water features on the bore free surface, with detailed quantitative and qualitative descriptions. Detailed air-water flow properties (void fraction and bubble size distributions) in a breaking roller were measured using phase-detection probes by Leng and Chanson (2019b,c). Shi et al. (2020) attempted to link the free-surface profiles with the air entrainment rate. Na et al. (2020) obtained providing velocity and vorticity data in an aerated roller of the spilling breakers, using both intrusive and non-intrusive techniques.

Overall, literature on turbulence characterisation in the breaking bore roller is thin. Thus, some of the present data were compared with those in hydraulic jumps of previous works, even though only a few studies focused on the turbulence in the hydraulic jump roller (Mortazavi et al., 2016; Kramer and Valero, 2020). Following a quasi-steady flow analogy, a breaking bore can be described as a hydraulic jump in translation (Lighthill, 1978; Peregrine and Svendsen, 1978). For a bore propagating on quiescent water, it exhibits a less turbulent process than a hydraulic jump, where the initial steady inflow brings additional source of turbulence into the roller (Yeh and Mok, 1990). Therefore, a tidal bore scenario, with the bore propagating on an opposite steady inflow, was selected to be comparative with the hydraulic jump.

The present study adopted an experimental approach to quantify the turbulence characteristics in a breaking bore roller, using novel image-based techniques. The present results are compared to those in tidal bore, hydraulic jump, swash zone bore and breaking wave with similar flow conditions. Section 2 presents experimental setup, instrumentation and signal processing. Section 3 and 4 show the velocity measurements and turbulence statistics respectively, and discussion is developed in Section 5. Conclusions are summarised in Section 6.

## 2. Experimental conditions, ensemble-averaging and signal processing

### 2.1. Experimental conditions

New experiments were conducted in a 19 m long and 0.7 m wide rectangular channel, with transparent glass sidewalls and a smooth PVC bottom (Fig. 2). The water was fed into the channel through an upstream intake tank equipped with flow calming devices, flow straighteners and a smooth convergent section. The flow rate was measured using a magneto flow meter with an accuracy of $10^{-5}$ $m^3/s$. A Tainter gate was located at downstream end of the channel at $x = 18.1$ m, where $x$ is the longitudinal distance from the upstream end (Fig. 2). The bore was generated by rapidly closing the Tainter gate, leading to an upstream bore propagation.

The bore propagation was recorded using a Phantom v2011 ultra-high-speed camera located at $x = 8.5$ m. The camera was equipped with a Nikkor 50 mm f/1.4 lens, focused about 14 mm from the glass sidewall with a depth of field (DOF) of 14 mm. The ultra-high-speed video movies were sampled at the maximum frame rate of 22,607 frame per second (fps) with a full HD resolution of 1 280 × 800 pixels. Herein, the ultra-high-speed videos were subsampled for every second frame, leading to a sampling frequency of 11,303 fps. A high-intensity LED array (GS Vitec MultiLED) with 4 × 6 lamps was used to illuminate the flow. Note that the LED was specifically manufactured for the Phantom camera with extremely high frequency to avoid flashing in the high-speed videos. The size of the image plane was 0.52 m long and 0.32 m wide (Fig. 2).

For quantitative comparisons with existing data in breaking rollers (Mortazavi et al., 2016; Leng and Chanson, 2019b,c), the present study adopted a breaking bore with a bore Froude number of $Fr_1 = 2.15$. The detailed flow conditions are presented in Table 1, where $d_1$ and $d_2$ are the initial and conjugate water depths respectively (Fig. 2), $Q$ is the flow rate, $V_1$ is the initial cross-sectional averaged velocity based on the continuity equation, $U$ is the average bore celerity measured using

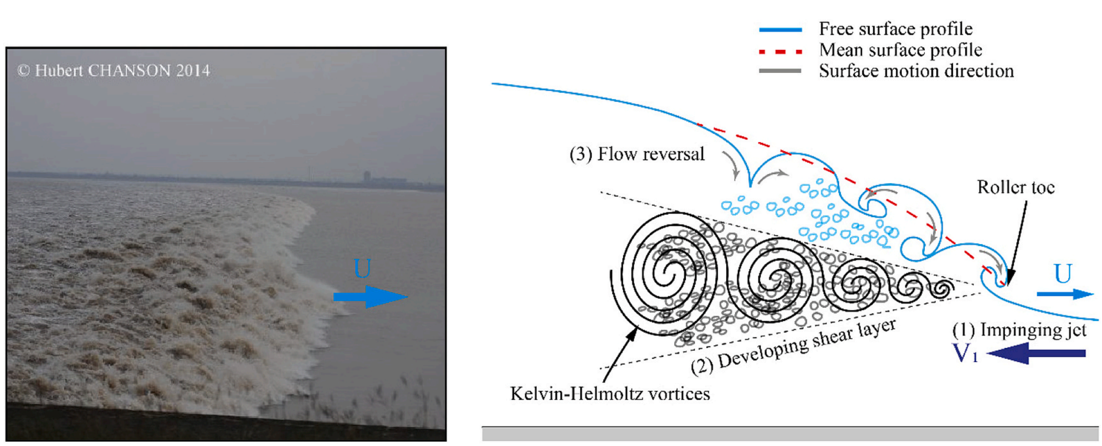


**Fig. 1.** Breaking bore advancing from left to right - Left: photograph of Qiantang bore, China by Prof. Hubert Chanson; Right: definition sketch of a breaking roller.

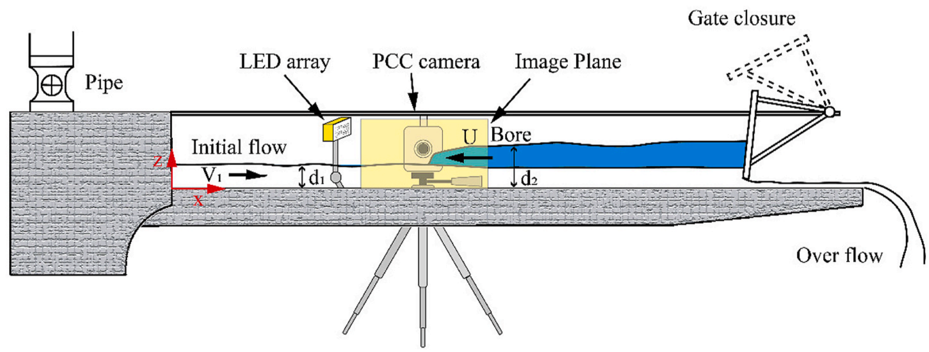


**Fig. 2.** Schematic of the present experimental setup and instrumentation.

**Table 1**
Flow conditions of the breaking bore.

| References | Type | $Fr_1$ [-] | $Re$ [−] | $Q$ [m$^3$/s] | $d_1$ [m] | $d_2$ [m] | $V_1$ [m/s] | $U$ [m/s] | Comment |
|---|---|---|---|---|---|---|---|---|---|
| Present study | Breaking bore | 2.15 | $2.03 \times 10^5$ | 0.100 | 0.097 | 0.244 | 1.458 | 0.627 | Physical modelling |
| Leng and Chanson (2019b,c) | Breaking bore | 2.15 | $2.03 \times 10^5$ | 0.100 | 0.097 | 0.244 | 1.458 | 0.627 | Physical modelling |
| Mortazavi et al. (2016) | Hydraulic jump | 2.00 | $1.10 \times 10^4$ | 0.036 | 0.056 | 0.129 | 2.700 | – | Numerical (DNS) data |

acoustic displacement meters (ADMs) over the measurement location, Re is the Reynolds number defined as $\rho(V_1 + U) \cdot d_1/\mu$, DNS stands for direct numerical simulation.

### 2.2. Optical flow technique

Optical flow (OF), as a well-established branch in computer revision, represents all kind of algorithms, which detect the apparent motions between consecutive frames based upon the brightness change. The reader is referred to the fundamentals of various OF techniques by Barron et al. (1994), and to the ranking systems of all the OF techniques by Middlebury (Baker et al., 2011), KITTI (Geiger et al., 2012) and MPI-Sintel (Butler et al., 2012).

Recently, several studies obtained dense two-dimensional velocity fields in various air-water flows (Bung and Valero, 2016a,b; Zhang and Chanson, 2019, 2018; Kramer and Chanson, 2019). These studies used the classic Horn-Schunck (HS) technique, Lucas-Kanade (LK) technique and Gunnar-Farneback (GF) technique, which provided the errors of 5–25% in air-water flows. Shi et al. (2020) examined these three techniques in a breaking bore. They suggested that none of them is ideal for turbulence characterisation, since the HS technique was sensitive to noise; the local averaging of LK technique would wipe off the turbulence; the governing equation of GF technique was lack of physical meaning in terms of brightness change. Hence, the present study adopted the "Classic + NL" (CNL) technique (Sun et al., 2010, 2014), which was derived from the HS technique with a high robustness of noise.

Several parameters affected the performance of the optical flow technique, including neighbourhood size, sampling frequency and pyramid level. The neighbourhood size is defined as a square N-by-N neighbouring pixels of the image where the objective functional is solved. The pyramid level is the level of the multi-resolution image pyramid technique (Adelson et al., 1984) for the detection of large displacements. The suitable parameters varied case by case, dependent on the OF technique, brightness and noise levels. Herein, the selections of these parameters were based on a sensitivity analysis (Appendix A and Supplementary material), and these parameters are summarised in Table 2.

### 2.3. Ensemble statistics analysis

For unsteady flows such as surface breaking flows, the time-averaged results are meaningless (Bradshaw, 1971), and an ensemble averaging

**Table 2**
Parameters used in the OF technique (Present study).

| Parameter [unit] | Adopted value |
|---|---|
| Neighbourhood [pixel × pixel] | 5 × 5 |
| Frame rate [fps] | 11,303 |
| pyramid level [−] | 7 |

has been commonly used in the literature. Herein, the ensemble averaging was achieved using an image-based algorithm of Shi et al. (2020), which automatically synchronised the positions of roller toe from different frames of an ultra-high-speed video movie at a reference location (Fig. 3). The accuracy of the synchronisation was examined by manually tracking the roller toe position (Appendix A). The reference position was selected based on two criteria: (1) most of the breaking roller could be observed from the image plane; (2) the number of frames was high enough to minimise the impacts of free-surface fluctuations on the ensemble statistics. In Appendix A, the sensitivity analysis on the number of frames suggested a minimum number of 20,000 frames. Herein, the reference point was selected as the 150th pixel from the right-edge of the image planes, ensuring 24,320 frames for ensemble statistical analyses.

## 3. Results. 1: ensemble-averaged velocity data

Near the boundaries of air-water flows where some random turbulent motions were observed, there was no aerated flow occupied in some frames. To avoid wiping off the turbulence information by using the same number of frames (24,320) across the entire image plane, the Kronecker delta $\delta_{ij}$ was used to describe the ensemble averaging:

$$V_i(x,z,t) = \frac{1}{N}\sum_{i=1}^{M} \delta_{ij} V_{ins,i}, \text{ where, } \delta_{ij} = \begin{cases} 0, & \text{if there is no aerated flow} \\ 1, & \text{if there is an aerated flow} \end{cases} \tag{2}$$

where $M$ is the total number of frames (24,300 herein), $N$ is the number of non-zero values at a given point, and $V_{ins,i}$ is the instantaneous velocity of frame $i$. This section presents the ensemble-averaged velocity fields and a self-similarity for the vertical profiles of longitudinal velocity data. The distribution on the number of frames used for ensemble statistics is presented in Appendix A.

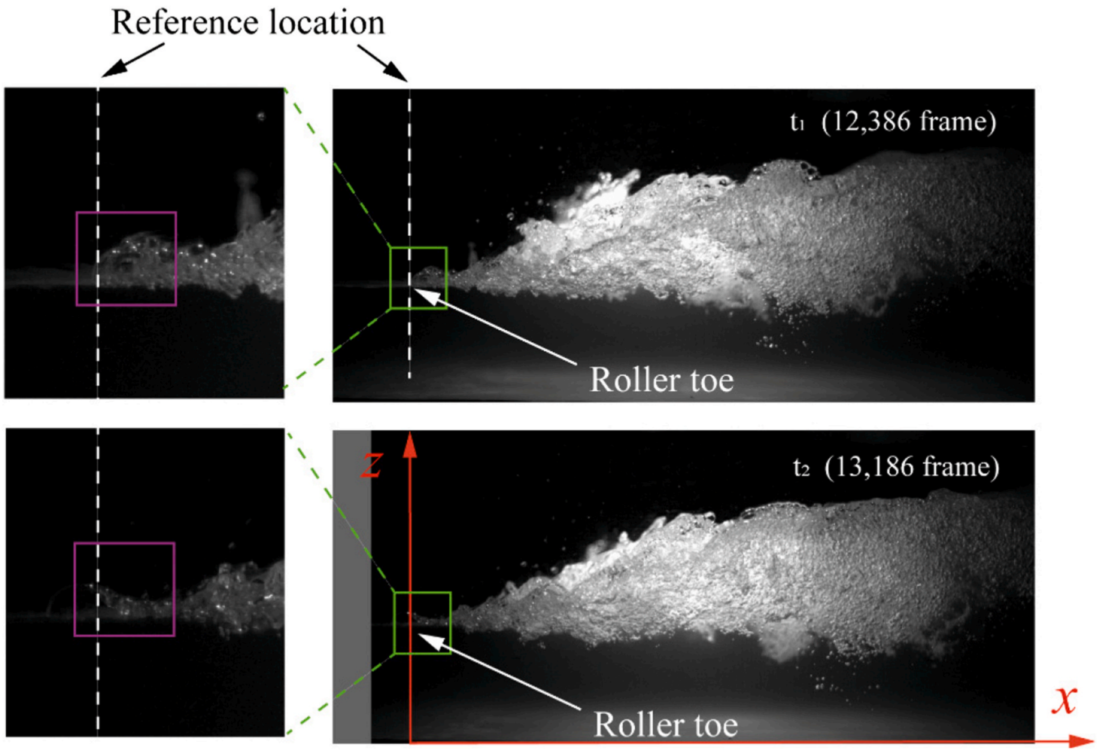


**Fig. 3.** Example of synchronisation process of the frame 12,386 and 13,186 in an ultra-high-speed video. The grey areas were added for the second image, ensuring the roller toes of the three images located at the reference point (the 150th pixel from the left image edge).

### 3.1. Two-dimensional velocity field

The breaking roller was classified into three regions based upon the longitudinal velocity data: (1) an *impinging jet* region, inducing air cavity and vorticity at the impingement point; (2) a *developing shear layer* region that is responsible for the air entrainment, bubble diffusion and vortex advection; (3) a *flow reversal* region driving the bore propagation (Fig. 1b). The dimensionless ensemble-averaged longitudinal velocity field in the breaking roller is presented in Fig. 4a. Note that the bore propagated from the right to left in Fig. 4. For the longitudinal velocity data (Fig. 4a), the impinging jet region exhibited relatively high velocity near the impingement point at the roller toe ($\underline{V_x}/V_1 = 0.4$–$0.6$), and the flow decelerated with an increase in longitudinal distance from the roller toe. The flow reversal region (blue region in Fig. 4a) exhibited negative dimensionless velocity ranging from $-0.6$ to $-0.2$, linked to the bore propagation in the opposite direction to the initial flow. The shear layer developed downstream of the impinging jet region, showing a broadening with increasing longitudinal distance from roller toe. A definition sketch of the three flow regions is shown in Fig. 4d. The vertical velocity data are presented in Fig. 4b, showing positive upward velocity data at the roller toe, consistent with the sudden increase in water depth during the bore propagation. Downward motions were observed immediate downstream of the roller toe, corresponding to a plunging process. Positive vertical velocity data for $(x\text{-}x_{toe})/d_1 > 3.0$ indicated that the buoyancy overcame the centrifugal pressure gradient induced from large-scale vortices, driving an upward bubbly flow motion. The ensemble-averaged vector field is presented in Fig. 4c. The flow pattern appeared similar to the velocity vector fields in the spilling breaker (Na et al., 2020, Fig. 5), in the hydraulic jump (Lin et al., 2012, Fig. 7) and for the uprush phase of swash zone bore (Cowen et al., 2003, Fig. 4), suggesting similar physical processes among these surface-breaking flows.

Furthermore, using a quasi-steady flow analogy, the breaking bore data were translated using the bore celerity for comparisons with the available data in stationary hydraulic jumps:

$$V_T = V_x - U \tag{3}$$

where $U$ is the mean bore celerity measured using acoustic displacement meters (ADMs). Fig. 5a presents the longitudinal velocity profiles from an Eulerian frame of reference. The present data were compared to the DNS results (Mortazavi et al., 2016) and bubble image velocimetry (BIV) data (Lin et al., 2012) for $Fr_1 = 2.0$ and 4.51 respectively in stationary hydraulic jumps. The air-water boundaries are plotted as reference in Fig. 5. The breaking bore data agreed well with the DNS data, except for the regions next to the air-water boundaries where the large fluctuations of air-water boundaries, affected the accuracy of ensemble averaging. Errors were induced next to the air-water boundaries, where the brightness consistency constraint of the OF technique was invalid because of the significant variation in the brightness data. The comparison between the bore data and BIV data showed a comparable order of magnitude, but the profile shape did not agree well, likely because of the large difference in Froude number: $Fr_1 = 4.51$ in Lin et al. (2012).

A comparison of present vertical velocity profiles with the DNS data (Mortazavi et al., 2016) is presented in Fig. 6. The results showed a reasonable agreement, although differences were observed next to the roller toe $(x\text{-}x_{toe})/d_1 < 2.0$, where the OF data indicated a downward motion, inconsistent with the DNS data. For hydraulic jump, the downward motion was observed in several works (Lin et al., 2012; Kramer and Valero, 2020), corresponding to a marked flow recirculation. The differences were likely caused by the much lower Reynolds number of the DNS model (an order of magnitude less than the present breaking bore). For the hydraulic jumps with similar Reynolds numbers as the DNS model, Bayon et al. (2016) showed no existence of the recirculation region. Furthermore, the present data agreed with the BIV data in terms of magnitude and trend (Appendix B).

### 3.2. Self-similarity of longitudinal velocity profiles in breaking bore roller

In the breaking roller, the free-shear layer developed downstream of

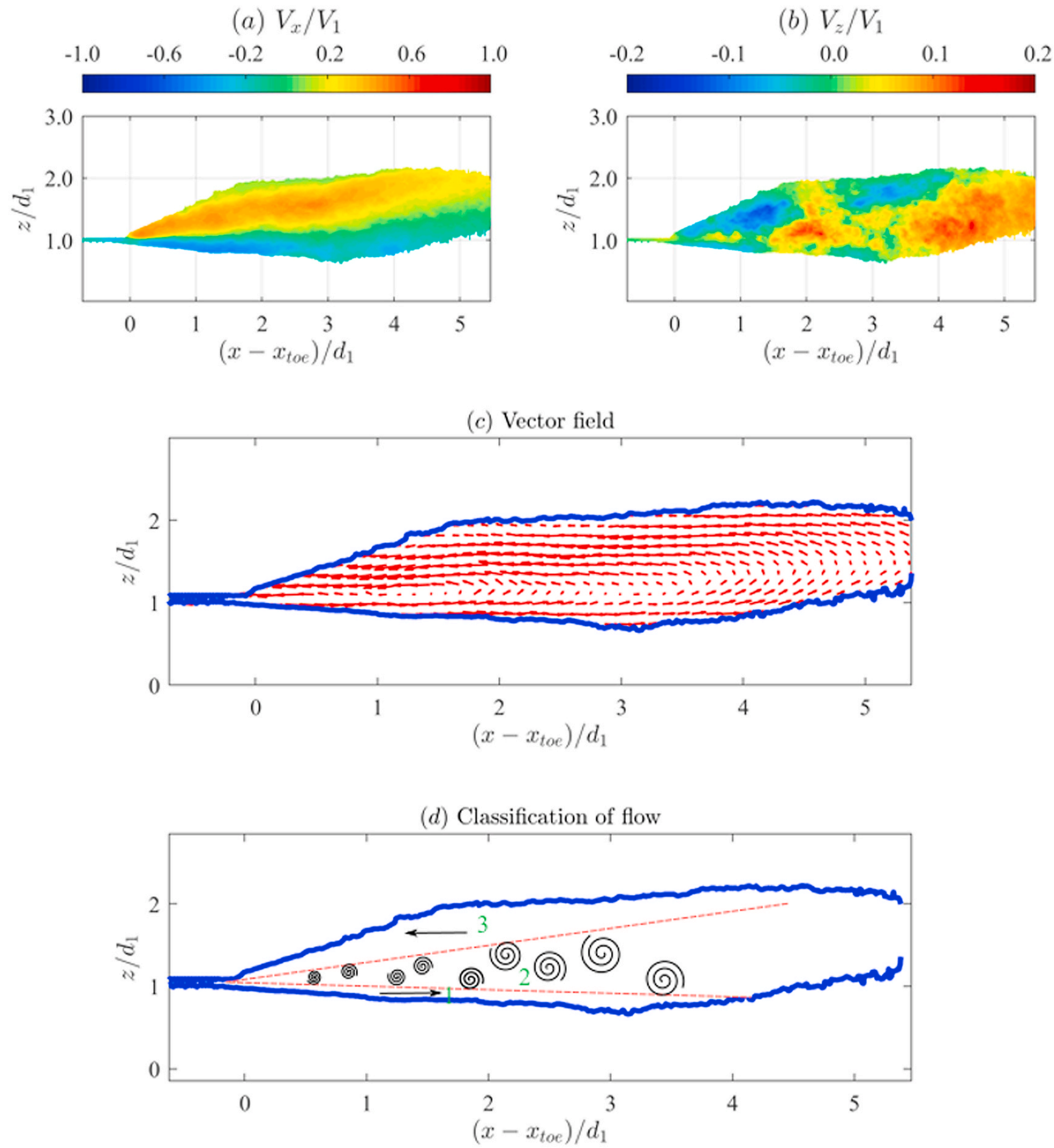


**Fig. 4.** Ensemble-averaged longitudinal and vertical velocity fields using the optical flow technique. The initial flow travelled from the left to the right, with the bore propagating in the opposite direction - (*a*): longitudinal velocity; (*b*): vertical velocity; (*c*): vector field; (*d*): classification of flow structure in breaking roller, with (1) *impinging flow*, (2) *developing shear mixing layer* and (3) *flow reversal* regions.

the singularity of the roller toe (Chanson and Brattberg, 2000; |Lin et al., 2012). Herein, the self-similarity of the vertical profile of longitudinal velocity was investigated in the developing shear layer. The vertical profile of the ensemble-averaged longitudinal velocity was normalised by its maximum and minimum velocities ($V_{x,max}$ and $V_{x,min}$), and its vertical coordinate was scaled by the vertical locations of $V_{x,max}$ and $V_{x,min}$ ($z_{x,max}$ and $z_{x,min}$) (Fig. 5b):

$$V_c = \frac{V_x - V_{x,\min}}{V_{x,\max} - V_{x,\min}}, \quad z_c = \frac{z - z_m}{z_{x,\min} - z_{x,\max}} \tag{4}$$

where $z_m$ is the difference between $z_{x,max}$ and $z_{x,min}$. The normalised ensemble-averaged profiles are presented in Fig. 7a, showing a self-similarity for all the velocity profiles, except for a few inconsistencies next to the air-water flow boundaries. The self-similar velocity profile may be expressed using a Fourier series:

$$V_c = 1 - [a_1 + a_2 \sin(a_3 z_m) + a_4 \cos(a_3 z_m)] \tag{5}$$

where $a_1 = 0.5$, $a_2 = 0.41$, $a_3 = 3.2$ and $a_4 = -0.26$ for the present study. Equation (5) is plotted in Fig. 7a. The vertical locations of maximum, minimum and zero longitudinal velocity data ($z_{x,max}$, $z_{x,min}$ and $z_{x,zero}$ respectively) are shown in Fig. 7b. The difference between $z_{x,min}$ and $z_{x,max}$ increased with increasing longitudinal distance from the roller toe, indicating a broadening of the shear layer away from the roller toe.

## 4. Results. 2: turbulence statistics

### *4.1. Reynolds stresses*

The velocity fluctuations were obtained from the instantaneous velocity fields: $v_{ins,i} = V_{ins,i} - V_i$, where $V_i$ is the instantaneous ensemble-averaged velocity (Eq. (2)). The Reynolds stresses characterised the momentum transport induced by the fluctuating velocities in the breaking roller. For the two-dimensional measurements, the ensemble-averaged Reynolds stresses $\tau_{ij}$ was defined as:

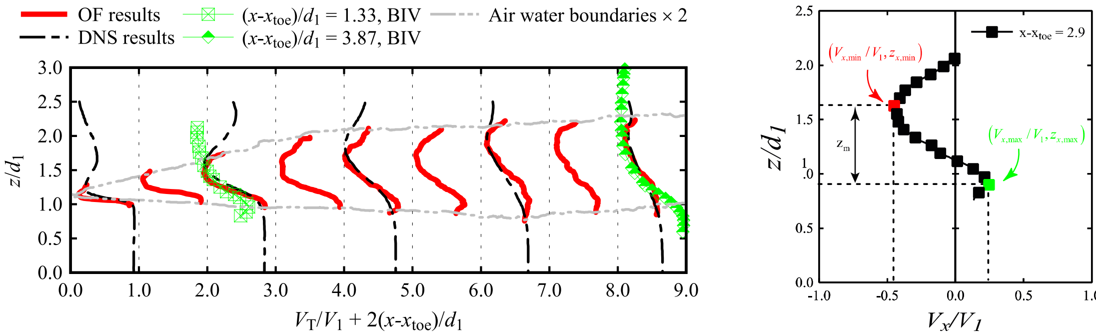


(*a*) (*b*)

**Fig. 5.** Ensemble-averaged longitudinal velocity profiles: (*a*) translate velocity profiles at different longitudinal locations $(x\text{-}x_{\text{toe}})/d_1 = 0.0$, 0.5, 1.0, 1.5, 2.0, 2.5, 3.0, 3.5 and 4.0, in comparison with the DNS data in hydraulic jump (Mortazavi et al., 2016) and with the BIV data in hydraulic jump (Lin et al., 2012); (*b*) an example of self-similar longitudinal velocity profile at $(x\text{-}x_{\text{toe}})/d_1 = 2.9$.

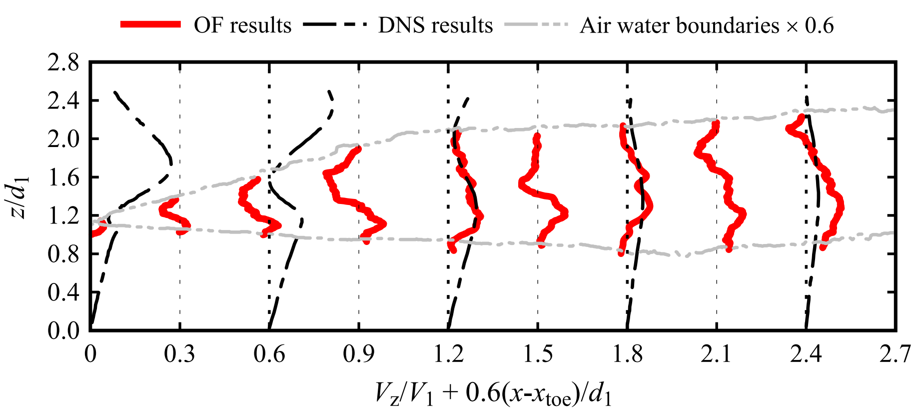


**Fig. 6.** Vertical velocity profiles at different longitudinal locations: $(x\text{-}x_{\text{toe}})/d_1 = 0.0$, 0.5, 1.0, 1.5, 2.0, 2.5, 3.0, 3.5 and 4.0, in comparison with data in a hydraulic jump (Mortazavi et al., 2016).

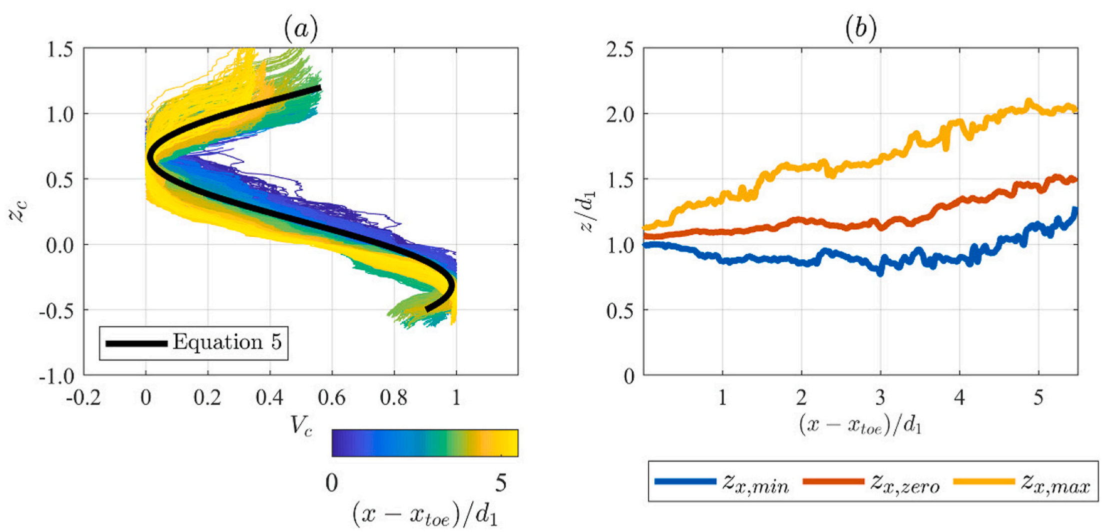


**Fig. 7.** Self-similarity of the ensemble-averaged longitudinal velocity profiles- (*a*) total 1 130 profiles from the roller toe and Equation (5) plotted for reference; (*b*): vertical locations of the minimum, zero and maximum ensemble-averaged longitudinal velocity profiles.

$$\frac{\tau_{ij}}{\rho V_1^2} = \begin{bmatrix} v_x v_x & v_x v_z \\ v_z v_x & v_z v_z \end{bmatrix} \Big/ V_1^2 \tag{6}$$

Fig. 8 presents the normalised ensemble-averaged Reynolds stress components: $v_x v_x/V_1^2$, $v_x v_z/V_1^2$, and $v_z v_z/V_1^2$, showing the same order of magnitude ($10^{-2}$). The streamwise normal stress $v_x v_x$ was the primary Reynolds stress with a larger magnitude than the $v_x v_z$ and $v_z v_z$ data. This finding suggested an anisotropic turbulent process immediately

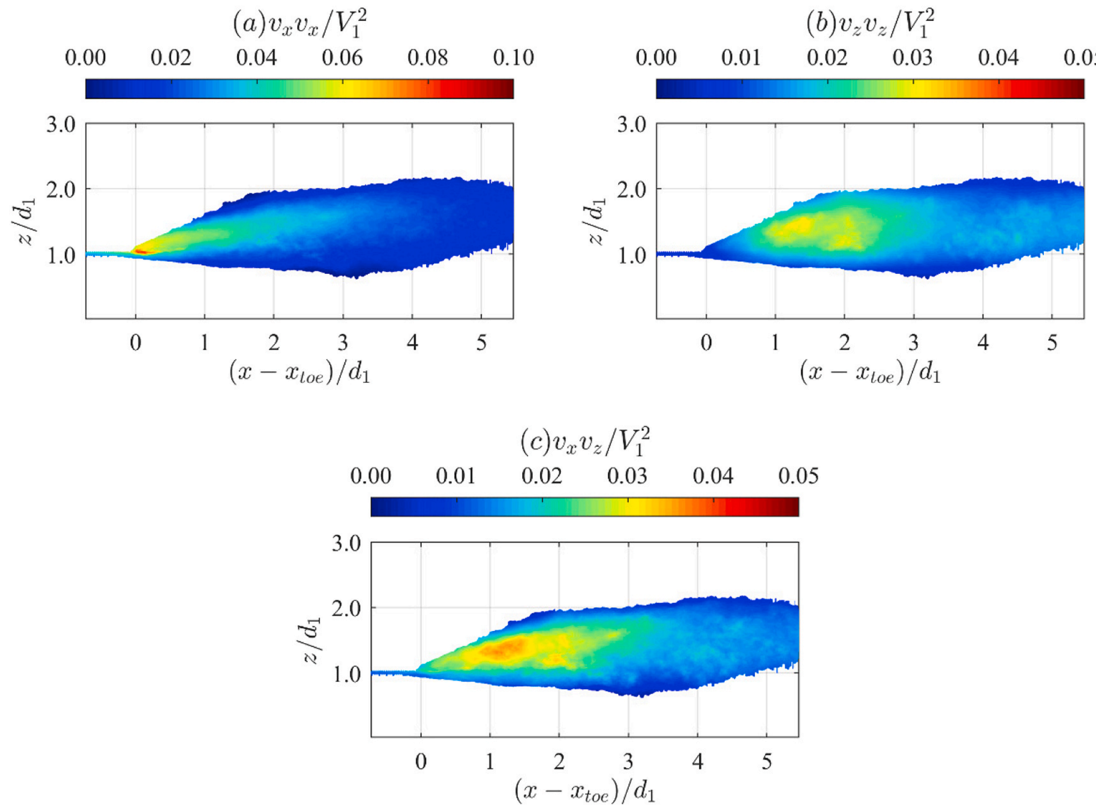


**Fig. 8.** Ensemble-averaged Reynold stresses and turbulent kinetic energy - (*a*): normal stress $v_xv_x$; (*b*): normal stress $v_zv_z$; (*c*): tangential stress $v_xv_z$.

downstream of the roller toe, which was caused by the high flow rotation in this region (Rogallo and Ferziger, 1985)., The Reynold stress data tended to decrease with increasing longitudinal distance. The order of magnitude of the present data were consistent with Reynolds stress data beneath a tidal bore (Leng and Chanson, 2019a), a swash zone bore (Cowen et al., 2003) and hydraulic jumps (Lin et al., 2012; Mortazavi et al., 2016; Witt et al., 2018).

The vertical profiles of ensemble-averaged Reynolds stresses at the different longitudinal locations are presented in Fig. 9. The longitudinal stress component exhibited a marked peak immediately downstream of the roller toe. For all the stresses, the profile tended to flatten with increasing longitudinal distance from the toe. For a given location further downstream ($(x\text{-}x_{toe})/d_1 \geq 3$), the values of three Reynolds stresses were close to each other, indicating that the turbulent flow became more isotropic. This might be caused by the dissipation of Kelvin–Helmholtz-type large-scale vortices further downstream. The present data quantitatively agreed well with the DNS data in a hydraulic jump with $Fr_1 = 2.0$ (Mortazavi et al., 2016) (Fig. 9).

A typical vertical profile of longitudinal Reynold stress and its key parameters are presented in Fig. 9a - Right, including the maximum and minimum Reynold stresses ($v_iv_{i,\max}$ and $v_iv_{i,\min}$) as well as their vertical locations ($z_{v_iv_i,\max}, z_{v_iv_i,\min}$). The present Reynolds stress data were best-fitted, for the longitudinal locations ($(x\text{-}x_{toe})/d_1 > 1.0$), using a power function (Mortazavi et al., 2016):

$$v_iv_{i,c} = \frac{z_{v_iv_i,c}}{\left(z_{R,m}/d_1\right)^{\beta}} \tag{7}$$

where $z_{R,m}$ is the difference between $z_{v_iv_i,\max}$ and $z_{v_iv_i,\min}$(Fig. 9a - Right), β is the power coefficient obtained from best-fitting ($\beta = 0.5$ in the present study), $v_iv_{i,c}$and $z_{v_iv_i,c}$are the characteristic Reynold stress and characteristic vertical coordinate respectively:

$$v_iv_{i,c} = \frac{v_iv_i - v_iv_{i,\min}}{v_iv_{i,\max} - v_iv_{i,\min}} z_{v_iv_i,c} = \frac{z - z_{v_iv_i,\max}}{d_1} \tag{8}$$

Fig. 10 presents the characteristic Reynolds stresses as functions of the characteristic vertical coordinate for the three stress components. The data exhibited similar C shapes.

### 4.2. *Vorticity and turbulent kinetic energy dissipation rate*

The breaking next to the roller toe was the source for vortex generation (Peregrine, 1983). Several vortex generation mechanics, based on shear layer instabilities, were discussed by Hornung et al. (1995) and Lubin et al. (2019). Herein, the instantaneous ensemble-averaged spanwise vorticity was derived from the strain rate of the instantaneous velocities as:

$$\varpi_y = \frac{1}{N}\sum_{i=1}^{N}\left(\frac{\partial V_{ins,z}}{\partial x} - \frac{\partial V_{ins,x}}{\partial z}\right) \tag{9}$$

Figs. 11a–1 presents the dimensionless ensemble-averaged vorticity magnitude data, consistent with the results in hydraulic jumps by Mortazavi et al. (2016) and Witt et al. (2018). The present vorticity magnitude data in breaking roller were approximately twice of those underneath the breaking roller, which were measured with the same flow conditions by Leng and Chanson (2019c). A relatively large vorticity magnitude was observed immediately downstream of the roller toe. The data showed some decaying vorticity away from the roller toe, consistent with a vortex-shedding phenomenon (Mortazavi et al., 2016). The maximum vorticity magnitude data are plotted as a function of longitudinal distance in Figs. 11a–2. The results indicated a peak in maximum vorticity magnitude immediately downstream of the roller toe about ($(x\text{-}x_{toe})/d_1 = 0.35$).

For the two-dimensional image-based techniques (PIV, BIV and OF), the elements of fluctuating velocity gradients related to the transversal direction could not be measured, thus resulting into assumptions of isotropic turbulence for the estimation of TKE dissipation rate (Liu et al., 2004; Xu and Chen, 2013). Considering sidewall effects on the flow from

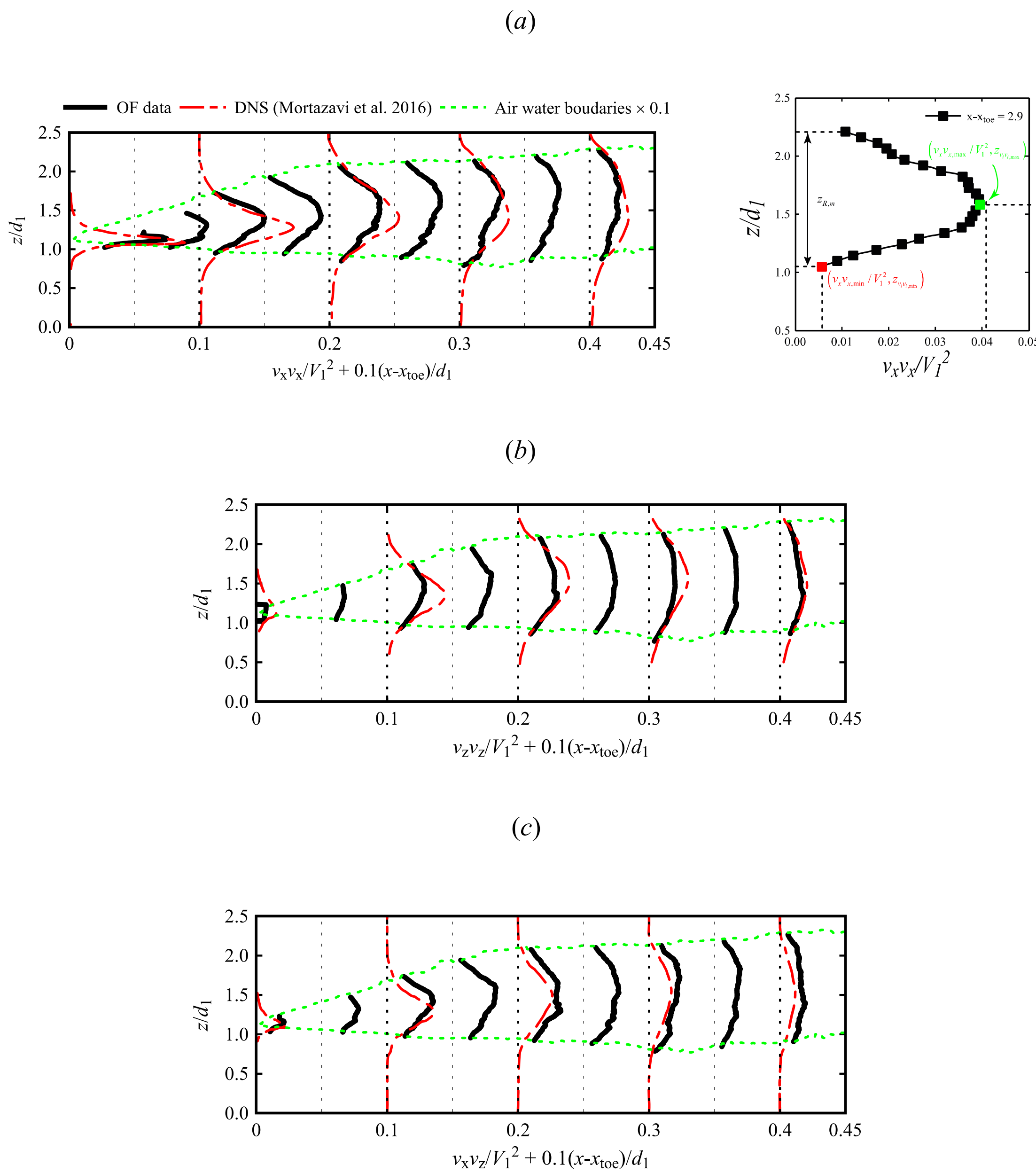


**Fig. 9.** Vertical profiles of ensemble-averaged Reynolds stresses at different longitudinal locations, in comparison to DNS data (Mortazavi et al., 2016) at $(x\text{-}x_{toe})/d_1 = 0.0, 1.0, 2.0, 3.0$ and $4.0$ - (*a*): normal stress (Right) with an example of a vertical profile (Left); (*b*): normal stress; (*c*): tangential stress.

the ultra-high-speed videos, the present TKE dissipation rate was estimated using a local isotropy assumption (Doron et al., 2001):

$$\varepsilon = \frac{1}{N}\nu\sum_{i=1}^{N}\left[4\left(\frac{\partial v_{ins,x}}{\partial x}\right)^2 + 4\left(\frac{\partial v_{ins,z}}{\partial z}\right)^2 + 3\left(\frac{\partial v_{ins,x}}{\partial z}\right)^2 + \ldots \right.$$
$$\left. 3\left(\frac{\partial v_{ins,z}}{\partial x}\right)^2 + 4\left(\frac{\partial v_{ins,x}}{\partial x}\frac{\partial v_{ins,z}}{\partial z}\right) + 6\left(\frac{\partial v_{ins,x}}{\partial z}\frac{\partial v_{ins,z}}{\partial x}\right)\right] \tag{10}$$

where $\nu$ is the kinematic viscosity of the fluid, $v_{ins,x}$, $v_{ins,z}$ are the instantaneous longitudinal and vertical velocity fluctuations respectively. Equation (10) was adopted in swash zone spilling waves (Huang et al., 2009). Note that the kinematic viscosity in the breaking bore varied based on the local void fraction, which was unable to measure in this present study. Thus, the kinematic viscosity of water was adopted in the roller.

Figs. 11b–1 presents the dimensionless ensemble-averaged TKE dissipation rate. The data agreed well with the results of hydraulic jumps (Mortazavi et al., 2016) and the bore formed from spilling breaker (Huang et al., 2009), in terms of both trend and order of magnitude. The maximum dissipation happened in the roller front region, with the maximum TKE dissipation rate observed next to the roller toe. This was consistent with the remarks of Lamarre and Melville (1991) and Lim et al. (2015), who suggested a higher energy dissipation for the breaking process at the wave front. The maximum TKE dissipation rate is plotted as a function of the longitudinal location in Figs. 11b–2. The peak value of the maximum TKE dissipation rate occurred at $(x\text{-}x_{toe})/d_1 = 0.33$, where the peak of vorticity magnitude occurred (Figs. 11a–2). In Figs. 11b–2, the data are compared to the results by Witt et al. (2018), who simulated a hydraulic jump of $Fr_1 = 2.43$ using unsteady RANS with k - ε turbulence closure model. The comparison showed that the RANS data were larger than the present data next to the roller toe, and some good agreement was seen for $(x\text{-}x_{toe})/d_1 > 1.8$. A further comparison of vertical profiles by Mortazavi et al. (2016) is shown in Fig. 12, showing a reasonable agreement in terms of the trend and order of magnitude.

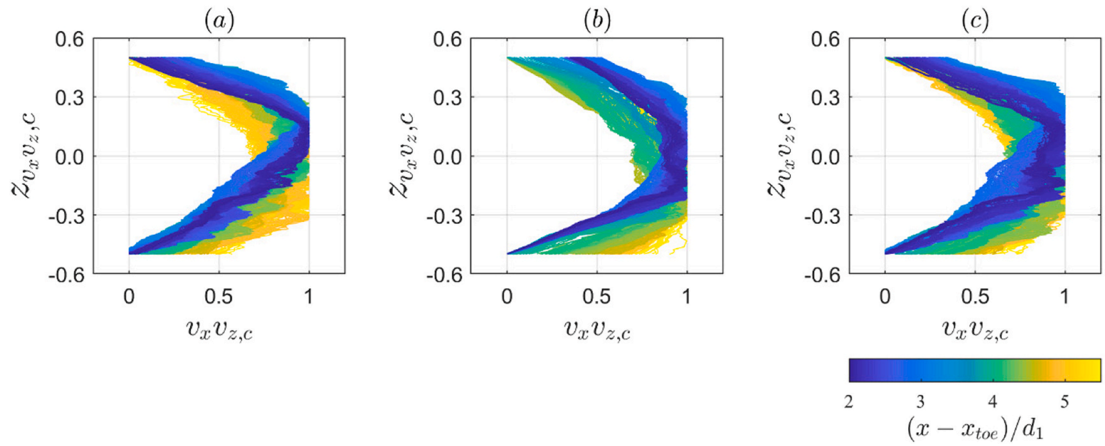


**Fig. 10.** Scaled ensemble-averaged Reynolds stresses for $(x\text{-}x_{toe})/d_1 > 1.0$. For each stress component, 893 profiles are plotted. - ($a$): normal stress $v_x v_x$; ($b$): normal stress $v_z v_z$; ($c$): tangential stress $v_x v_z$.

Herein, large differences were mostly seen in the roller toe region. The cause was the different estimations of the TKE dissipation rate. The present dissipation rate data were derived from a two-dimensional measurements, while Witt et al. (2018) and Mortazavi et al. (2016) computed the TKE dissipation rate from three-dimensional measurements. Near the roller toe, the flow was likely inhomogeneous and anisotropic owing to the Kelvin-Helmholtz type of instability (Lázaro and Lasheras, 1989), and strong turbulence was observed along the roller toe perimeter in the transverse direction (Wüthrich et al., 2020a). Furthermore, the comparison of the TKE dissipation rate between the two numerical studies provided large differences for a hydraulic jump with similar Froude number ($Fr_1 = 2.4$). The comparison highlighted good agreement in the downstream region of the roller at roller, where the flow became more isotropic. Therefore, above discussions suggested that the inconsistent TKE dissipation rate data might be caused by the highly anisotropic flow near the roller toe, leading to more advanced

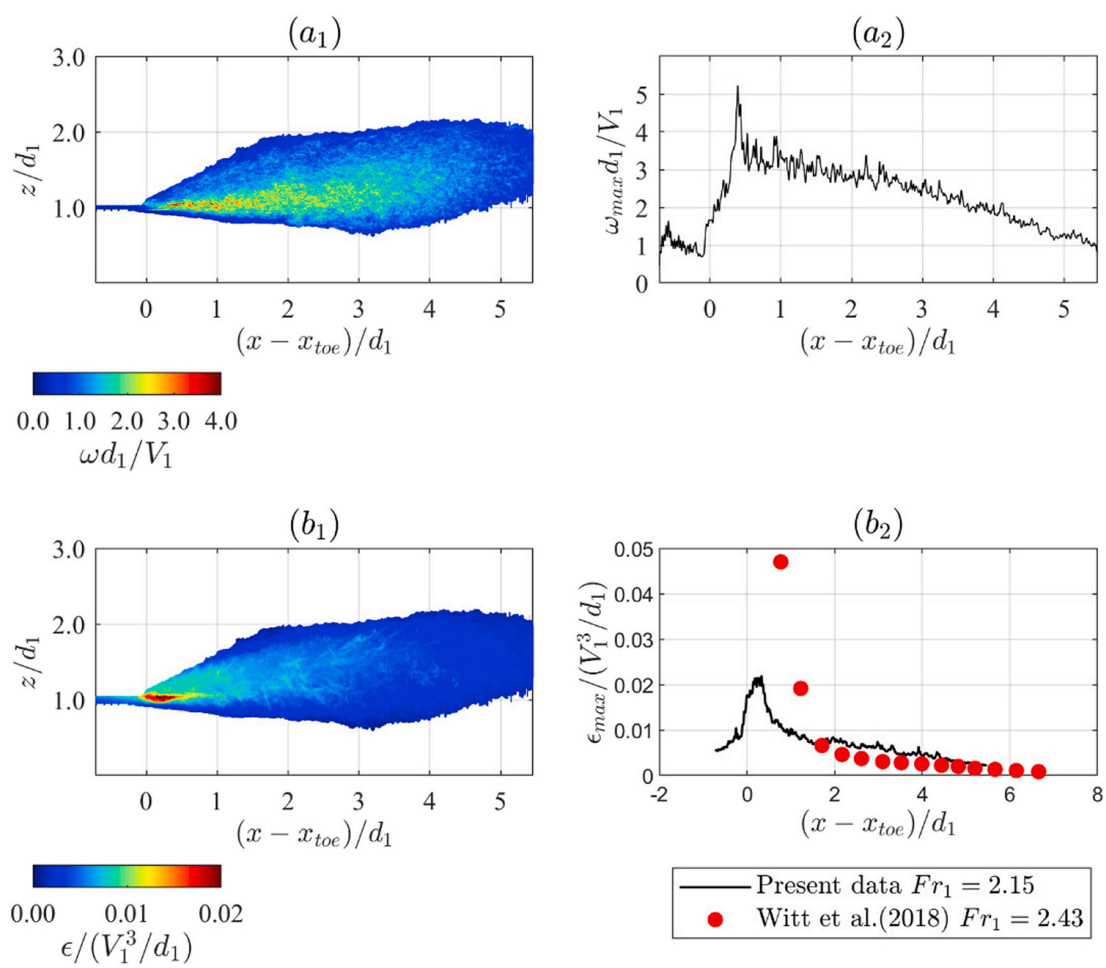


**Fig. 11.** Ensemble-averaged turbulence statistics ($a_1$): vorticity magnitude distribution; ($a_2$): maximum vorticity magnitude of vertical profile; ($b_1$): TKE dissipation rate distribution; ($b_2$): maximum TKE dissipation rate of vertical profile.

numerical and theoretical models on TKE dissipation rate in the future.

### 4.3. Integral turbulent time and length scales

The integral turbulent length and time scales provided characteristic dimension and duration of the coherent structures in the production range (Pope, 2000). In the present study, the integral turbulent length and time scales were obtained from the temporal and spatial cross-correlation functions of the velocity fluctuations (Hinze, 1975). Detailed illustrations are shown in Appendix C.

The ensemble-averaged dimensionless integral turbulent length and time scales in both longitudinal and vertical directions are presented in Fig. 13. The data were not valid for $(x\text{-}x_{toe})/d_1 > 4.8$, because of the insufficient separation distance for the integration of spatial cross-correlation. Overall, the present distributions were comparable to single-point probe measurements in hydraulic jumps (Wang et al., 2014, Fig. 8). A common region of relatively small dimensionless turbulent length and time scales was observed in Fig. 13 (blue regions), with the order of the magnitude ($10^{-2}$) being consistent with the data in breaking waves (Pedersen et al., 1998), in hydraulic jumps (Wang et al., 2014). In this region, the high TKE dissipation rate (Fig. 11) resulted into low Kolmogorov length and time scales ($\eta$ and $\tau_\eta$), where $\eta = (\nu^3/\varepsilon)^{1/4}$ and $\tau_\eta = (\nu/\varepsilon)^{1/2}$ with $\nu$ is the kinematic viscosity of the fluid (Kolmogorov, 1941). The combination of large integral turbulent scales and small Kolmogorov scales might facilitate the energy transfer through a short inertial subrange, thus resulting into high energy dissipation near the roller toe. Note that the present study was not able to estimate Kolmogorov scales, since $\nu$ value varied with the void fraction in the air-water flow. Furthermore, the turbulent length and time scales tended to increase with an increase in longitudinal distance. In the flow reversal region, large time and length scales were observed (orange colour), where the coherent structures interacted with free-surface fluctuations of low frequencies (Wang, 2014). Further downstream in the roller $(x\text{-}x_{toe})/d_1/d_1 = 4$–5, large integral turbulent length scale corresponded to small integral turbulent time scale. This might indicate a three-dimensional advection of turbulence structures in the breaking roller.

The longitudinal turbulent integral length and time scales were approximately twice as large as those in the vertical direction, indicating that the large-scale vortices were stretched in the longitudinal direction. An alternative turbulent time scale was derived from the auto-correlation function of the velocity fluctuations. The comparison between integral turbulent time scale and auto-correlation time scale showed a good agreement (Appendix C).

## 5. Discussion

The turbulence generated at the roller toe had significant impacts on the bubble dynamics in the breaking roller, including bubble advection, bubble size-distributions, bubble breakups and bubble coalescences. A discussion between present turbulence data and existing air-water properties is thus developed, attempting to link turbulence to the bubble dynamics in the breaking roller.

### 5.1. Vorticity and bubble clustering

The ultra-high-speed videos highlighted that the large-scale vortical structures entrapped bubbles, and advected them downstream. The interaction between the turbulent vortices and air bubbles led to a non-random bubble grouping by inertia forces, namely bubble clustering (Sene et al., 1994). There are limited experimental data on bubble clustering in breaking bores (Leng and Chanson, 2019b). On the other hand, several experimental works provided detailed bubble clustering properties in hydraulic jumps (Wang et al., 2015). Although the investigation of air-water properties in breaking bores was not the focus of the present study, the consistent trends between the present vorticity data in breaking bores and the clustering data in hydraulic jumps are worth to discuss. Wang et al. (2015) showed that both number of bubble clusters and average number of bubbles in clusters exhibited marked peaks immediately downstream of the roller toe, and decreased with increasing longitudinal distance. These findings were consistent with the present vorticity distributions in Figs. 11a–1. In the shear layer, the longitudinal decrease in the percentage of bubbles in clusters (Chachereau and Chanson, 2011) was similar with the trend of the maximum vorticity (Figs. 11a–2).

### 5.2. Dissipation rate and bubble size distributions

The violent air-water flow motion in the breaking roller dissipated a portion of the total dissipated energy, as much as 15–30% for vortex advection (Sawaragi and Iwata, 1974), 40% and 50% for bubble-turbulence and bubble-bubble interplay (Lamarre and Melville, 1991). Several studies showed a link between turbulent dissipation and bubble size distributions (Hinze, 1955; Lasheras et al., 1999a,b; Garrett et al., 2000). Herein, the Hinze scale (Hinze, 1955), defined as the minimum bubble size which bubbles no longer break down by turbulence due to surface tension, was estimated based upon the maximum dissipation rate of the vertical profiles:

$$D_H = C\left(\frac{\sigma}{\rho}\right)^{3/5} \varepsilon_{\max}{}^{(-2/5)} \tag{11}$$

where $C = 0.725$ is a constant, $\sigma$ and $\rho$ are the surface tension and water density respectively. The Hinze scale data are presented in Fig. 14. The Hinze scale decreased immediately downstream of the roller toe, and increased with increasing longitudinal distance. Despite the intrinsic limitation of Equation (11) (Hinze, 1975, p. 394), the present findings were consistent with previous data (Witt et al., 2018). The current smallest Hinze scale was 4.4 mm at $(x\text{-}x_{toe})/d_1 = 0.35$, larger than that of Mortazavi et al. (2016) ($D_H = 2.4$ mm).

Hinze (1955) indicated that 95% of air mass was contained in the bubbles with the diameter smaller than $D_H$. The present largest Hinze scale was 10.92 mm, consistent with 95% of bubble chord length distribution ($L_{ch,95}$) in a breaking bore roller by Leng and Chanson (2019b). Furthermore, the present Hinze scale data were compared to existing $L_{ch,95}$ data in hydraulic jumps (Chachereau and Chanson, 2010, 2011; Wang, 2014) at the same location in Table 3. The comparison showed a reasonable agreement between present and existing bubble size data, although the data of Chachereau and Chanson (2010,2011) showed a relatively larger maximum bubble size immediately downstream of the roller toe. Their large maximum bubble size might be associated with the presence of large air pockets entrapped at the roller toe. In Table 3, the $L_{ch,95}$ data were independent on the Froude number.

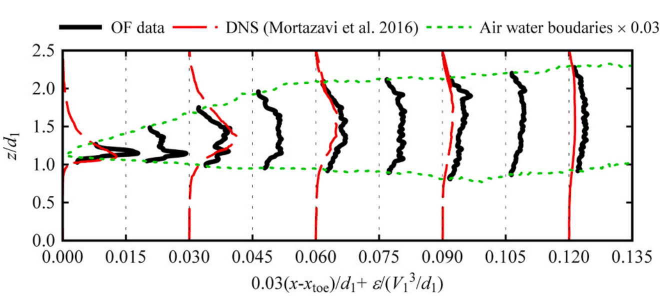


**Fig. 12.** Vertical profiles of turbulence kinetic energy dissipation rate at different longitudinal locations, in comparison with the DNS data (Mortazavi et al., 2016).

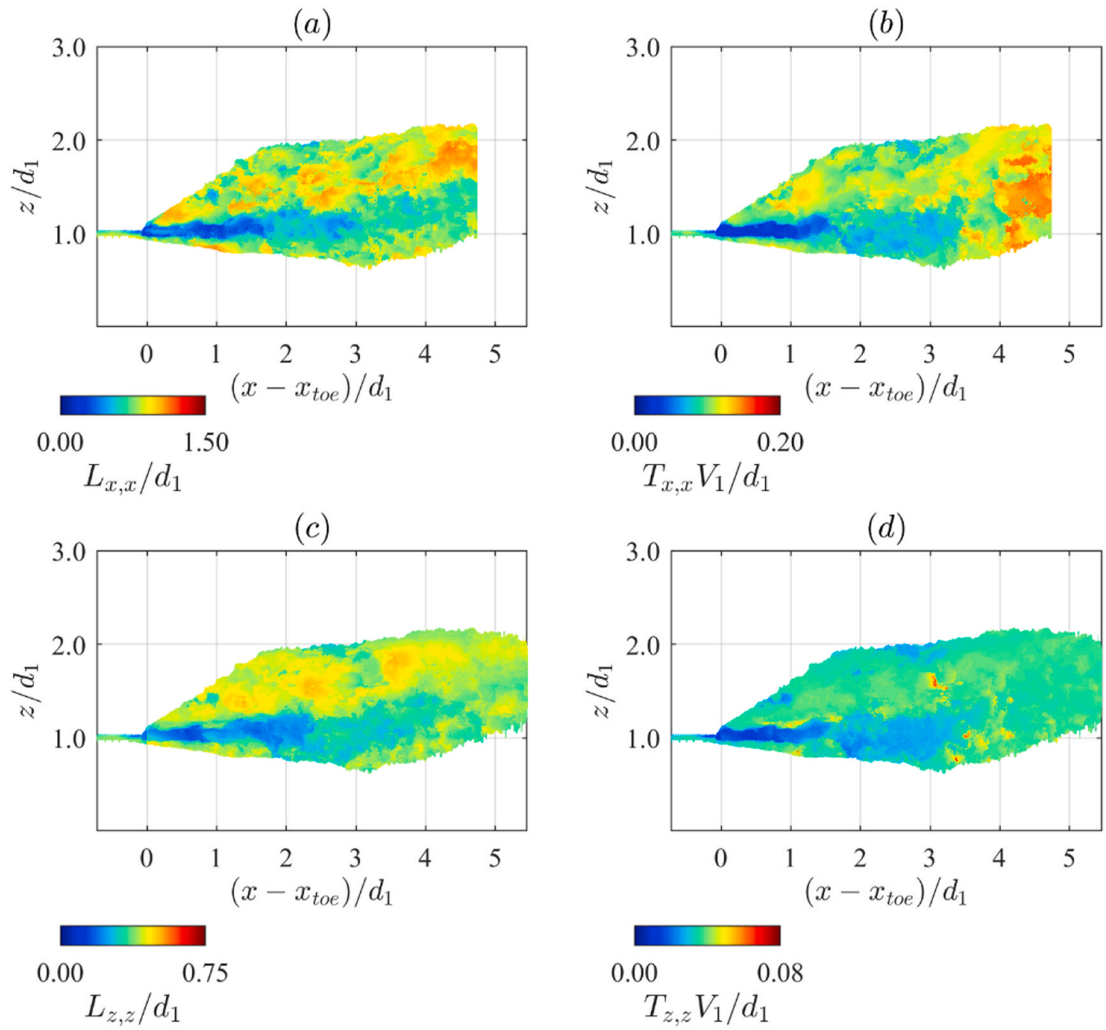


**Fig. 13.** Ensemble-averaged integral turbulent scales based on 23 videos- (*a*): longitudinal integral turbulent length scale; (*b*): longitudinal integral turbulent time scale; (c): vertical integral turbulent length scale; (*d*): vertical integral turbulent time scale.

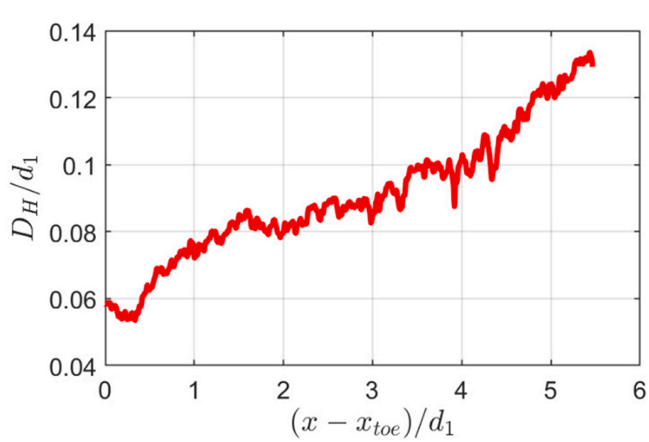


**Fig. 14.** A conservative estimation of Hinze scale using the maximum TKE dissipation rate data of vertical profiles.

**Table 3**
Comparison between the present Hinze scale and previous chord length data.

| References | $Fr_1$ | Locations | Existing data $L_{ch,95}$ [mm] | Present data $D_H$ [mm] |
|---|---|---|---|---|
| Chachereau and Chanson (2010, 2011) | 3.1 | $(x\text{-}x_{toe})/d_1 = 0.90$; $y/d_1 = 1.23$ | >10 | 6.47 |
| | 3.1 | $(x\text{-}x_{toe})/d_1 = 1.70$; $y/d_1 = 1.14$ | >10 | 6.89 |
| | 3.1 | $(x\text{-}x_{toe})/d_1 = 3.41$; $y/d_1 = 1.46$ | 8–9 | 7.82 |
| | 3.8 | $(x\text{-}x_{toe})/d_1 = 1.81$; $y/d_1 = 1.14$ | >10 | 8.04 |
| | 3.8 | $(x\text{-}x_{toe})/d_1 = 3.61$; $y/d_1 = 1.21$ | 9–10 | 10.08 |
| Wang (2014) | 5.1 | $(x\text{-}x_{toe})/d_1 = 4.15$; $y/d_1 = 1.35$ | 6.75–7 | 8.57 |

## 6. Conclusion

The current study presents an experimental study of a breaking bore for a Froude number $Fr_1 = 2.15$ and Reynolds number $\mathrm{Re} = 2.3 \times 10^5$, with a focus on the breaking roller. The flow field was recorded using an ultra-high-speed video camera, sampled at 22,607 fps with full HD resolution. The high-speed videos were subsampled to 11,303 fps based upon a sensitivity analysis, and post-processed using an optical flow (OF) technique to obtain the instantaneous velocity fields. A synchronisation technique was developed, and the ultra-high-speed video recordings were repeated 23 times, thus enabling ensemble statistical flow properties over 24,300 frames. The present results were compared to existing data obtained in breaking bores, in hydraulic jumps based upon a quasi-steady flow analogy and in breaking waves.

Based on the ensemble-averaged velocity fields, the breaking bore roller was classified into three regions, namely the impinging region, developing shear layer and flow reversal region. The ensemble-averaged velocity data compared well with DNS results in a stationary hydraulic jump, and the velocity vector field agreed with the vector fields in breaking waves and a swash zone bore. A self-similarity of the ensemble-averaged longitudinal velocity was found by scaling using the width of the shear layer.

The ensemble-averaged Reynolds stress data showed that the longitudinal component ($v_x v_x$) was twice as large as other components ($v_z v_z$ and $v_x v_z$) next to the roller toe ($(x\text{-}x_{toe})/d_1 < 2.0$), indicating an anisotropic turbulent flow in this region. The stress data quantitatively agreed well with existing data in hydraulic jumps and breaking bores. Away from the roller toe, the stress components tended to approach isotropic conditions with increasing distance from the roller toe. The Reynolds stress profiles did not hold self-similarity, and they were best fitted by a power function. The high vorticity data next to the roller toe corresponded to the vortex generation by the breaking events, leading to some vortex-shedding further downstream. The turbulent kinetic energy dissipation rate was estimated using the velocity fluctuation data. The physical dimension and duration of coherent structures in the $x$-$z$ plane were characterised in terms of the integral turbulent length and time scales. Both length and time scale data in the developing shear layer and next to the roller toe were at least one order of magnitude smaller than data in other regions, corresponding to the rapid evolution of the Kelvin-Helmoltz-type vortices. The large time and length scales in the flow reversal region might relate to some vortices coupling with the free-surface fluctuations of low frequency.

A discussion was developed linking the turbulence measurements with the air-water flow properties. The present vorticity data exhibited consistent trends with previously reported bubble clustering properties. Hinze scale data, representing the maximum bubble size, were derived using the dissipation rate data. The results compared well with the bubble chord length distributions in previous studies.

Overall, this study leads to a better understanding of the unsteady turbulent processes in a breaking bore roller. The comparison of present and existing data suggested similar physical processes in air-water flow region among the tidal bore, hydraulic jump, swash zone bore and breaking wave. The present study was limited to a two-dimensional turbulence analysis, while three-dimensional flow properties need to be further examined in the future. A meaningful extension of the work would use an array of phase-detection probes to obtain the ensemble-averaged turbulence and air-water measurements based on numerous repetitions.

## Author Statement

Rui Shi: Conceptualization, Methodology, Software, Formal analysis, Visualization, Writing - Original Draft, Project administration. Xinqian Leng: Conceptualization, Methodology, Writing - Review & Editing, Supervision. Hubert Chanson: Conceptualization, Methodology, Writing - Review & Editing, Supervision.

## Declaration of competing interest

The authors declare that they have no known competing financial interests or personal relationships that could have appeared to influence the work reported in this paper.

## Acknowledgments

The authors acknowledge the technical supports from Jason Van Der Gevel, Steward Matthews and Dr Van Thuan Nguyen (The University of Queensland). They also acknowledge the helpful comment from Professor Ali Mani (Stanford University).

## Appendix D. Supplementary data

Supplementary data to this article can be found online at https://doi.org/10.1016/j.coastaleng.2021.103893.

## Appendix A. Measurement accuracy

### *A-1 Optical flow*

The OF parameters played important roles on the results, thus a sensitivity analysis was required to obtain suitable values. However, there was a lack of validation dataset in the breaking bore from the literature, owing to the inherent difficulties for measuring flow properties in aerated air-water flows experimentally. Therefore, the sensitivity analysis was conducted in a steady plunging air-water jet, and the details are presented in the Supplementary Material.

### *A-2 Synchronisation*

The position of the roller toe detected by the synchronisation technique was crucial for the estimation of turbulent properties. To examine the impacts of the synchronisation process on the results, the roller toe positions were manually tracked based on the brightness data induced by the sudden increase water level at bore front. The comparisons between manual tracking and image-based technique are presented in Figure A-1, showing a good agreement. Furthermore, the synchronisation might be critical near the roller toe, where velocity in gradients were large and integral length and time scales were small. Thus, the ensemble-averaged flow properties were obtained near the roller toe $(x\text{-}x_1)/d_1 = 0.5$, using the roller toe positions of both manual and automatic tracking, as presented in Figure A-2. Overall, the data exhibited a good agreements between image-based and manual synchronisations.

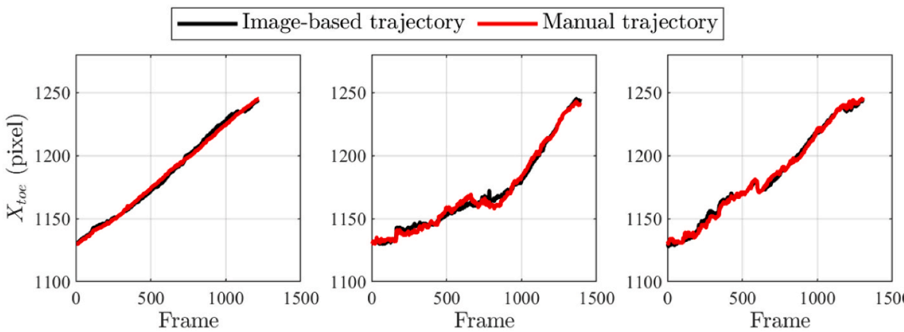


**Fig. A-1.** Comparisons between roller toe positions using image-based and manual detections for three ultrahigh-speed videos.

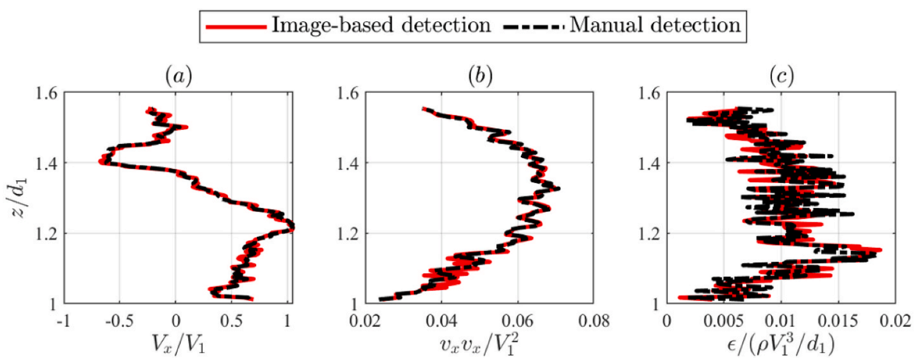


**Fig. A-2.** Dimensionless ensemble statistics using the roller toe positions of image-based and manual detections: (*a*) longitudinal velocity profiles; (*b*) normal Reynolds stress in longitudinal direction (c) TKE dissipation rate. 1 100 frames from 1 video were used for ensemble averaging.

## *A-3 Number of frames*

A sensitivity analysis was conducted to investigate the impact of the number of frames on the ensemble statistics. The ensemble-averaged velocity fields using 100, 1,000, 10,000, 15,000, 20,000 and 23,000 frames are presented in Figure A-3, where (e) and (f) exhibited almost no differences. This suggested a minimum number of 20,000 frames for ensemble-averaging.

Violent flow motions were obtained from the high-speed videos, leading to constantly varied bore shape. At a location near the free surface, there was sometimes no flow. To avoid wiping off the turbulence information, only the pixels that had the flow was taken for ensemble-averaging, which resulted into less used frames near boundaries of aerated region. Figure A-4 showed that at least 15,000 frames were used near the averaged air-water flow boundaries.

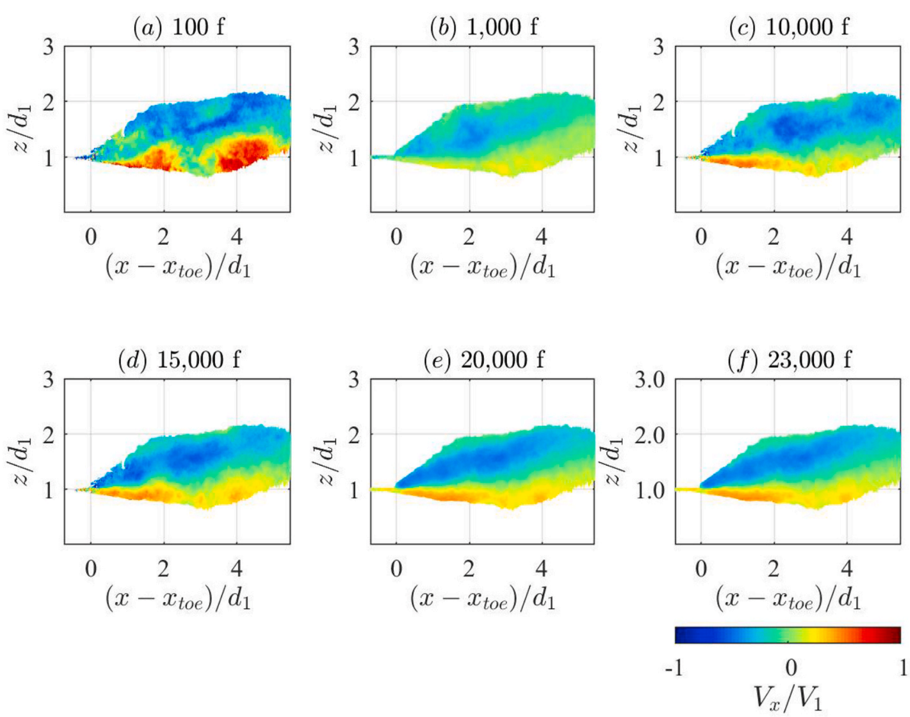


**Fig. A-3.** Sensitivity analysis on the number of frames used to compute ensemble-averaged longitudinal velocity distributions, where f means frames.

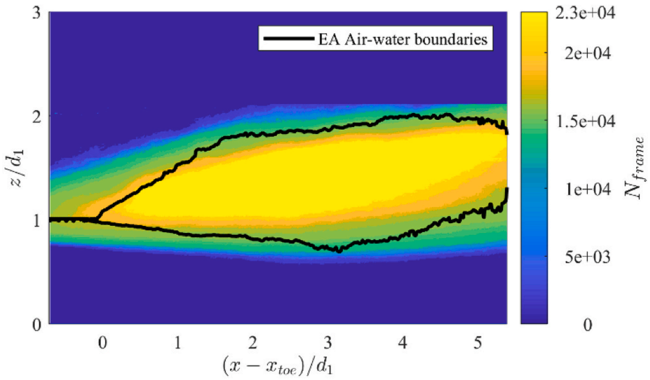


**Fig. A-4.** Distributions of the number of frames used for ensemble statistics, based on 23,000 frames.

## Appendix B. Vertical velocity comparison

Further comparison of the vertical velocity was done between the present data and the BIV results in stationary hydraulic jump with $Fr_1 = 4.51$ (Lin et al., 2012). Unexpectedly, the comparison highlighted a good agreement for the vertical profiles at the same dimensional longitudinal positions, though the two studies had different flow conditions (Figure B-1). This suggested that the vertical motion was independent on the flow conditions.

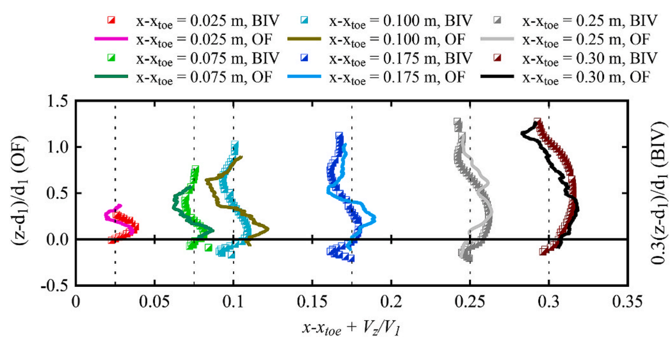


**Fig. B-1.** Comparison of vertical velocity profiles between the present study and profiles obtained from BIV measurements at the same dimensional longitudinal positions while the Froude number are different.

## Appendix C. Integral turbulent time and length scales

### C-1 Presentation

For a time series of a velocity fluctuation component $v_i(t)$, the normalised auto- and cross-correlation function $R_{ix}$ was defined as (Pope, 2000):

$$R_i(\tau) = \|v_i(t)v_i(t+\tau)\| \tag{C-1}$$

$$S_{i,i}(\tau) = \left\|v_{i,n}(t)v_{i,m}(t+\tau)\right\| \tag{C-2}$$

where $v_{i,n}(t)$ and $v_{i,m}(t)$ are the velocity fluctuations at longitudinal locations m and n respectively, $\tau$ is the time lag, and operator || || means a normalisation process. Figure C-1 presents a typical example of longitudinal velocity fluctuation signals, auto-and cross-correlation functions. The auto- and cross-correlation time scales were calculated as (Figure C-1b and c):

$$T_{i,R} = \int_0^{\tau(R_i=0)} R_i(\tau)d\tau \tag{C-3}$$

$$T_{i,S} = \int_{\tau\left(S_{i,i}=\left(S_{i,i}\right)_{\max}\right)}^{\tau\left(S_{i,i}=0\right)} S_{i,i}(\tau)d\tau \tag{C-4}$$

The integral turbulent length scales represents the dimension of the coherent turbulent structures (Hinze, 1975). The cross-correlation function of $v_i(t)$ signals at two points with a separation distance $\Delta L_i$, where $i = x$ and $z$, provided the integral turbulent length scale (Figure C-2). The maximum cross-correlation coefficient $(S_{i,i})_{\max}$ can be written as a function of the separation distance, and the longitudinal and vertical integral turbulent length and time scales were calculated as:

$$L_{i,i} = \int_{0}^{\Delta L_i\left(\left(S_{i,i}\right)_{\max}=0\right)} \left(S_{i,i}\right)_{\max} d(\Delta d_i) \tag{C-5}$$

$$T_{i,i} = \frac{1}{L_{i,i}} \int_{0}^{\Delta L_i\left(\left(S_{i,i}\right)_{\max}=0\right)} \left(S_{i,i}\right)_{\max} T_{i,S} d(\Delta d_i) \tag{C-6}$$

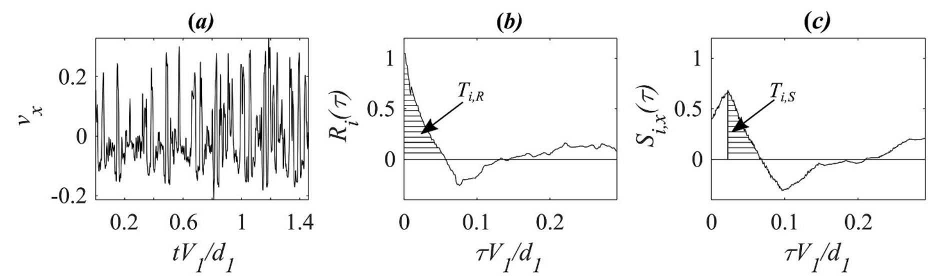


**Fig. C-1.** Typical example of longitudinal velocity fluctuation signal and its normalised auto- and cross-correlation functions at $(x\text{-}x_{toe})/d_1 = 0.38$ (near the roller toe) and $z/d_1 = 1.0$: (*a*) velocity fluctuations as a function of time lag; (*b*): auto-correlation function; (*c*): cross-correlation function between $(x\text{-}x_{toe})/d_1 = 0.38$ and 0.39.

Figure C-3 illustrates a typical example of integral length scale calculation based on the present experimental data. The maximum cross-correlation coefficient as a function of the separation distance might have a long "tail" with an increase in separation distance, and might increase after a consequent delay. In such cases, the integration stopped at the first maximum cross-correlation coefficient less than 0.2 if the next five maximum cross-correlation coefficients ranged between 0.1 and 0.2, or if the next five maximum cross-correlation coefficients provided a positive average gradient. Then the integration included the area of a small triangle, based on the average decreasing gradient (green shaded triangle in Figure C-3b).

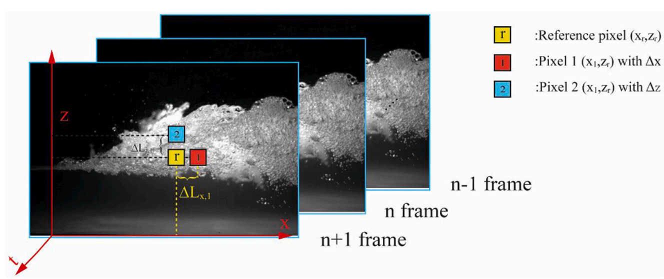


Figure C-2. Illustration of longitudinal and vertical separation distances used for integral turbulent length and time scales.

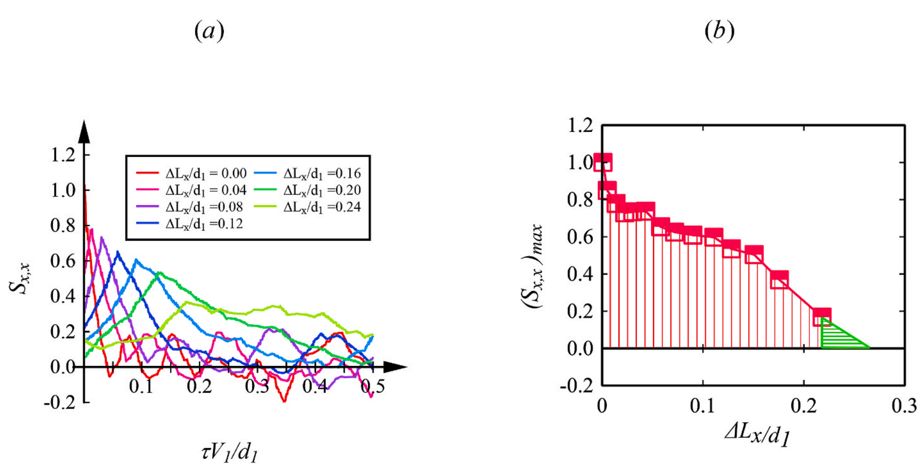


**Fig. C-3.** Illustration of integral turbulent time scale - (*a*): cross-correlation functions with an increase in longitudinal separation distance $\Delta L_x$; (*b*): maximum cross-correlation coefficient as a function of longitudinal separation distance. Reference pixel location: $(x\text{-}x_{toe})/d_1 = 1.1$ and $z/d_1 = 1.0$.

*C-2 Auto-correlation time scale*

The auto-correlation time scale represented a typical lifespan of turbulent structures, and was calculated using Equation C-3. The longitudinal and vertical auto-correlation time scales are presented in Figure C-4. In the developing shear mixing layer region, the auto-correlation time scale data were one order of magnitude less near the roller toe than in other regions, with an increase with increasing longitudinal distance. The finding hints small turbulence structures formed at the roller toe, and paired while being advected downstream. The smaller turbulence structures were expected to dissipate larger amount of turbulence kinetic energy, consistent with the results shown in Fig. 11. Large auto-correlation time scale data were observed in the flow reversal region. The difference between the auto-correlation time scales of $v_x$ and $v_z$ suggested that the advection of turbulent structures was a three-dimensional process in the breaking roller. Both auto-correlation time scale and integral turbulent time scales were in the same order of magnitude, and shared some common trends. Small differences were observed, likely linked to the different definitions.

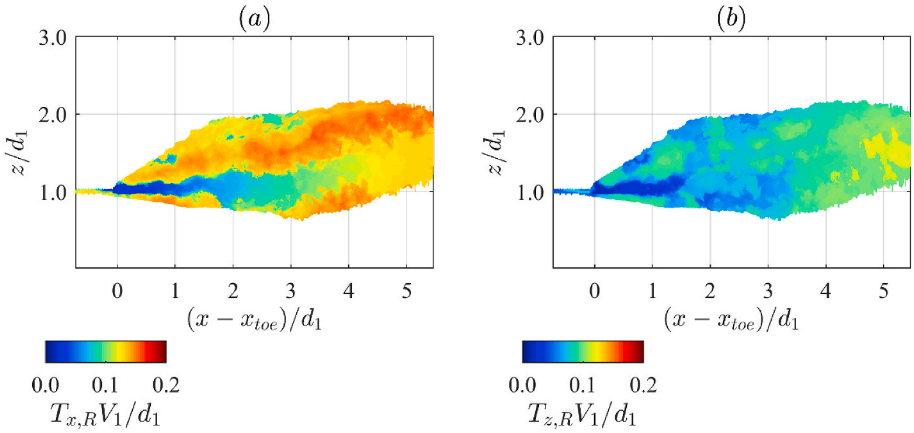


**Fig. C-4.** Ensemble-averaged auto-correlation time scales based on 23 videos - (*a*): longitudinal velocity component; (*b*): vertical velocity component.

## References


Adelson, E.H., Anderson, C.H., Bergen, J.R., Burt, P.J., Ogden, J.M., 1984. Pyramid methods in image processing. RCA engineer 29 (6), 33–41. In: https://scholar.google.com/scholar?hl=en&as_sdt=0%2C5&q=+Pyramid+methods+in+image+processing&btnG=.

Baker, S., Scharstein, D., Lewis, J.P., Roth, S., Black, M.J., Szeliski, R., 2011. A database and evaluation methodology for optical flow. Int. J. Comput. Vis. 92, 1–31. https://doi.org/10.1007/s11263-010-0390-2.

Barron, J.L., Fleet, D.J., Beauchemin, S.S., 1994. Performance of optical flow techniques. Int. J. Comput. Vis. 12 (1), 43–77.

Bayon, A., Valero, D., García-Bartual, R., Vallés-Morán, F.J., López-Jiménez, P.A., 2016. Performance assessment of OpenFOAM and FLOW-3D in the numerical modeling of a low Reynolds number hydraulic jump. Environ. Model. Software 80, 322–335. https://doi.org/10.1016/j.envsoft.2016.02.018.

Bradshaw, P., 1971. An Introduction to Turbulence and its Measurement, first ed. Pergamon, Oxford.

Brocchini, M., Peregrine, D.H., 2001. The dynamics of strong turbulence at free surfaces. Part 1. Description. J. Fluid Mech. 449, 225–254. https://doi.org/10.1017/S0022112001006012.

Bung, D.B., Valero, D., 2016a. Application of the optical flow method to velocity determination in hydraulic structure models. 6th Int. Symp. Hydraul. Struct. Hydraul. Struct. Water Syst. Manag 223–232. https://doi.org/10.15142/T3150628160853. ISHS 2016 3150628160.

Bung, D.B., Valero, D., 2016b. Optical flow estimation in aerated flows Daniel. J. Hydraul. Res. 54, 575–580. https://doi.org/10.1080/00221686.2016.1173600.

Butler, D.J., Wulff, J., Stanley, G.B., Black, M.J., 2012. A naturalistic open source movie for optical flow evaluation. In: Fitzgibbon, A., Lazebnik, S., Perona, P., Sato, Y., Schmid, C. (Eds.), Computer Vision-ECCV 2012. Springer, Berlin Heidelberg, pp. 611–625.

Chachereau, Y., Chanson, H., 2011. Bubbly flow measurements in hydraulic jumps with small inflow Froude numbers. Int. J. Multiphas. Flow 37, 555–564. https://doi.org/10.1016/j.ijmultiphaseflow.2011.03.012.

Chachereau, Y., Chanson, H., 2010. Free-Surface Turbulent Fluctuations and Air-Water Flow Measurements in Hydraulics Jumps with Small Inflow Froude Numbers, Hydraulic Model Report No. CH78/10. The University of Queensland, Australia, pp. 1–133.

Chanson, H., 2011. Tidal Bores, Aegir, Eagre, Mascaret, Pororoca Theory and Observations, first ed. World Scientific, Singpore. https://doi.org/10.1142/8035.

Chanson, H., Brattberg, T., 2000. Experimental study of the air-water shear flow in a hydraulic jump. Int. J. Multiphas. Flow 26, 583–607. https://doi.org/10.1016/S0301-9322(99)00016-6.

Cowen, E.A., Sou, I.M., Liu, P.L.F., Raubenheimer, B., 2003. Particle image velocimetry measurements within a laboratory-generated swash zone. J. Eng. Mech. 129, 1119–1129. https://doi.org/10.1061/(ASCE)0733-9399(2003)129:10(1119).

Doron, P., Bertuccioli, L., Katz, J., Osborn, T.R., 2001. Turbulence characteristics and dissipation estimates in the coastal ocean bottom boundary layer from PIV data. J. Phys. Oceanogr. 31, 2108–2134. https://doi.org/10.1175/1520-0485(2001)031<2108:tcadei>2.0.co;2.

Dressler, R.F., 1954. Comparison of theories and experiments for the hydraulic dam-break wave. Int. Assoc. Sci. Hydrol.

Garrett, C., Li, M., Farmer, D., 2000. The connection between bubble size spectra and energy dissipation rates in the upper ocean. J. Phys. Oceanogr. 30, 2163–2171. https://doi.org/10.1175/1520-0485(2000)030<2163:TCBBSS>2.0.CO;2.

Geiger, A., Lenz, P., Urtasun, R., 2012. Are we ready for autonomous driving? the KITTI vision benchmark suite. In: Proceedings of the IEEE Computer Society Conference on Computer Vision and Pattern Recognition. https://doi.org/10.1109/CVPR.2012.6248074.

Hinze, J.O., 1975. Turbulence McGraw-Hill. Publi, 2nd Edition. New York, USA.

Hinze, J.O., 1955. Fundamentals of the hydrodynamic mechanism of splitting in dispersion processes. AIChE J. https://doi.org/10.1002/aic.690010303.

Hornung, H.G., Willert, C., Turner, S., 1995. The flow field downstream of a hydraulic jump. J. Fluid Mech. 287, 299–316. https://doi.org/10.1017/s0022112095000966.

Huang, Z.C., Hsiao, S.C., Hwung, H.H., Chang, K.A., 2009. Turbulence and energy dissipations of surf-zone spilling breakers. Coast. Eng. 56, 733–746. https://doi.org/10.1016/j.coastaleng.2009.02.003.

Kiger, K.T., Duncan, J.H., 2012. Air-entrainment mechanisms in plunging jets and breaking waves. Annu. Rev. Fluid Mech. 44, 563–596. https://doi.org/10.1146/annurev-fluid-122109-160724.

Kolmogorov, A., 1941. The local structure of turbulence in incompressible viscous fluid for very large Reynolds numbers. Dokl. Akad. Nauk SSSR 30, 299–303. https://doi.org/10.1098/rspa.1991.0075.

Kramer, M., Chanson, H., 2019. Optical flow measurements in aerated spillway flows: validation and discussion on sampling processing parameters. Exp. Therm. Fluid Sci. 103, 318–328. https://doi.org/10.1016/j.expthermflusci.2018.12.002.

Kramer, M., Valero, D., 2020. Turbulence and self-similarity in highly aerated shear flows: the stable hydraulic jump. Int. J. Multiphas. Flow 129, 103316. https://doi.org/10.1016/j.ijmultiphaseflow.2020.103316.

Lamarre, E., Melville, W., 1991. Air entrainment and dissipation in breaking waves. Nature 351, 465.

Lasheras, J.C., Martínez-Bazán, C., Montañés, J.L., 1999a. On the breakup of an air bubble injected into a fully developed turbulent flow. Part 2. Size PDF of the resulting daughter bubbles. 30th Fluid Dyn. Conf. 401, 183–207. https://doi.org/10.2514/6.1999-3642.

Lasheras, J.C., Martínez-Bazán, C., Montañés, J.L., 1999b. On the breakup of an air bubble injected into a fully developed turbulent flow. Part I: breakup frequency. 30th Fluid Dyn. Conf. 401, 157–182. https://doi.org/10.2514/6.1999-3642.

Lázaro, B.J., Lasheras, J.C., 1989. Particle dispersion in a turbulent, plane, free shear layer. Phys. Fluids 1, 1035–1044. https://doi.org/10.1063/1.857394.

Leng, X., Chanson, H., 2019a. Two-dimensional integral turbulent scales in compression wave in a canal. Exp. Therm. Fluid Sci. 102, 163–180. https://doi.org/10.1016/j.expthermflusci.2018.09.014.

Leng, X., Chanson, H., 2019b. Flow Air-water interaction and characteristics in breaking bores. Int. J. Multiphas. Flow 120, 103101. https://doi.org/10.1016/j.ijmultiphaseflow.2019.103101.

Leng, X., Chanson, H., 2019c. Two-phase flow measurements of an unsteady breaking bore. Exp. Fluid 60. https://doi.org/10.1007/s00348-019-2689-2.

Leng, X., Chanson, H., 2016. Coupling between free-surface fluctuations, velocity fluctuations and turbulent Reynolds stresses during the upstream propagation of positive surges, bores and compression waves. Environ. Fluid Mech. 16, 695–719. https://doi.org/10.1007/s10652-015-9438-8.

Lighthill, M.J., 1978. Waves in Fluids, first ed. Cambridge University Press.

Lim, H.-J., Chang, K.-A., Huang, Z.C., Na, B., 2015. Experimental study on plunging breaking waves in deep water. J. Geophys. Res. Ocean. 120, 2007–2049. https://doi.org/10.1002/jgrc.20224.

Lin, C., Hsieh, S.C., Lin, I.J., Chang, K.A., Raikar, R.V., 2012. Flow property and self-similarity in steady hydraulic jumps. Exp. Fluid 53, 1591–1616. https://doi.org/10.1007/s00348-012-1377-2.

Liu, M., Rajaratnam, N., Zhu, D.Z., 2004. Turbulence structure of hydraulic jumps of low Froude numbers. J. Hydraul. Eng. https://doi.org/10.1061/(ASCE)0733-9429(2004)130:6(511).

Lubin, P., Kimmoun, O., Véron, F., Glockner, S., 2019. Discussion on instabilities in breaking waves: vortices, air-entrainment and droplet generation. Eur. J. Mech. B Fluid 73, 144–156. https://doi.org/10.1016/j.euromechflu.2018.05.006.

Madsen, P.A., Svendsen, I.A., 1983. Turbulent bores and hydraulic jumps. J. Fluid Mech. 129, 1–25. https://doi.org/10.1017/S0022112083000622.

Melville, W.K., Veron, F., White, C.J., 2002. The velocity field under breaking waves: coherent structures and turbulence. J. Fluid Mech. 454, 203–233. https://doi.org/10.1017/S0022112001007078.

Mortazavi, M., Le Chenadec, V., Moin, P., Mani, A., 2016. Direct numerical simulation of a turbulent hydraulic jump: turbulence statistics and air entrainment. J. Fluid Mech. 797, 60–94. https://doi.org/10.1017/jfm.2016.230.

Na, B., Chang, K.-A., Lim, H.-J., 2020. Flow kinematics and air entrainment under laboratory spilling breaking waves. J. Fluid Mech. 882, 1–36. https://doi.org/10.1017/jfm.2019.817.

Nadaoka, K., Hino, M., Koyano, Y., 1989. Structure of the turbulent flow field under breaking waves in the surf zone. J. Fluid Mech. 204, 359–387. https://doi.org/10.1017/S0022112089001783.

Pedersen, C., Deigaard, R., Sutherland, J., 1998. Measurements of the vertical correlation in turbulence under broken waves. Coast. Eng. 35, 231–249. https://doi.org/10.1016/S0378-3839(98)00044-1.

Peregrine, D., 1966. Calculations of development of an undular bore. J. Fluid Mech. 25, 321–330. https://doi.org/10.1017/S0022112066001678.

Peregrine, D.H., 1983. Breaking waves on beaches. Annu. Rev. Fluid Mech. 15, 149–178. https://doi.org/10.1146/annurev.fl.15.010183.001053.

Peregrine, D.H., Svendsen, I.B.A., 1978. Spilling breakers, bores and hydraulic jumps. Coast. Eng. 540–550.

Pope, S., 2000. Turbulent Flows. Cambridge Univ. Press, p. 771.

Rayleigh, Lord, 1908. Note on tidal bore. Proc. R. Soc. 81, 448–449.

Rogallo, R.S., Ferziger, J., 1985. Effect of rotation on isotropic turbulence: computation and modelling. J. Fluid Mech. 154, 321–336. https://doi.org/10.1017/S0022112085001550.

Sawaragi, T., Iwata, K., 1974. Turbulence effect on wave deformation after breaking. Coast. Eng. Japan 17, 39–49. https://doi.org/10.1080/05785634.1974.11924181.

Sene, K.J., Hunt, J.C.R., Thomas, N.H., 1994. The role of coherent structures in bubble transport by turbulent shear flows. J. Fluid Mech. 259, 219–240. https://doi.org/10.1017/S0022112094000108.

Shi, R., Leng, X., Chanson, H., 2020. On optical flow techniques applied to breaking surges. Flow Meas. Instrum. 101710 https://doi.org/10.1016/j.flowmeasinst.2020.101710.

Soares Frazao, S., Zech, Y., 2002. Undular bores and secondary waves -Experiments and hybrid finite-volume modelling. J. Hydraul. Res. 40, 33–43. https://doi.org/10.1080/00221680209499871.

Sun, D., Roth, S., Black, M.J., 2014. A quantitative analysis of current practices in optical flow estimation and the principles behind them. Int. J. Comput. Vis. 106, 115–137. https://doi.org/10.1007/s11263-013-0644-x.

Sun, D., Roth, S., Black, M.J., 2010. Secrets of optical flow estimation and their principles. IEEE Comput. Soc. Conf. Comput. Vis. Pattern Recogn. 2432–2439. https://doi.org/10.1109/CVPR.2010.5539939.

Wang, H., 2014. Turbulence Air Entrainment in Hydraulic Jumps. PhD Thesis. The University of Queensland. https://doi.org/10.14264/uql.2014.542.

Wang, H., Felder, S., Chanson, H., 2014. An experimental study of turbulent two-phase flow in hydraulic jumps and application of a triple decomposition technique. Exp. Fluid 55. https://doi.org/10.1007/s00348-014-1775-8.

Wang, H., Hu, Z., Chanson, H., 2015. Two-dimensional bubble clustering in hydraulic jumps. Exp. Therm. Fluid Sci. 68, 711–721. https://doi.org/10.1016/j.expthermflusci.2015.07.006.

Witt, A., Gulliver, J.S., Shen, L., 2018. Numerical investigation of vorticity and bubble clustering in an air entraining hydraulic jump. Comput. Fluids 172, 162–180. https://doi.org/10.1016/j.compfluid.2018.06.019.

Wüthrich, D., Pfister, M., Nistor, I., Schleiss, A.J., 2018. Experimental study of tsunami-like waves generated with a vertical release technique on dry and wet beds. J. Waterw. Port, Coast. Ocean Eng. 144, 04018006 https://doi.org/10.1061/(asce)ww.1943-5460.0000447.

Wüthrich, D., Shi, R., Chanson, H., 2020a. Physical study of the 3-dimensional characteristics and free-surface properties of a breaking roller in bores and surges. Exp. Therm. Fluid Sci. 112, 109980. https://doi.org/10.1016/j.expthermflusci.2019.109980.

Wüthrich, D., Shi, R., Chanson, H., 2020b. Air-water characteristics of a breaking bore roller. Part I: two-phase surface features and strong turbulence. Hydraul. Model Rep. No. CH117/20 1–119. ISBN: 798-1-74272-308–2.

Xu, D., Chen, J., 2013. Accurate estimate of turbulent dissipation rate using PIV data. Exp. Therm. Fluid Sci. 44, 662–672. https://doi.org/10.1016/j.expthermflusci.2012.09.006.

Yeh, H.H., 1991. Tsunami bore runup. Nat. Hazards. https://doi.org/10.1007/BF00162788.

Yeh, H.H., Mok, K., 1990. On turbulence in bores. Phys. Fluids A Fluid Dyn. 2, 821–828. https://doi.org/10.1063/1.857630.

Zhang, G., Chanson, H., 2019. Application of optical flow methods to aerated skimming flows above triangular and trapezoidal step cavities. J. Hydraul. Res. 57, 488–497. https://doi.org/10.1080/00221686.2018.1489900.

Zhang, G., Chanson, H., 2018. Application of local optical flow methods to high-velocity free-surface flows: validation and application to stepped chutes. Exp. Therm. Fluid Sci. 90, 186–199. https://doi.org/10.1016/j.expthermflusci.2017.09.010.

SHI, R., LENG, X., and CHANSON, H. (2021). " Breaking Bore Roller Characteristics: Turbulence Statistics Using Optical Techniques." *Coastal Engineering*, Vol. 168, Paper 103893, 17 pages & Suppl. data (DOI: 10.1016/j.coastaleng.2021.103893) (ISSN 0378-3839).

# Breaking Bore Roller Characteristics: Turbulence Statistics Using Optical Techniques - **Supplementary Material on Optical Flow Technique**

by Rui SHI ([1]), Xinqian LENG ([1,2]) and Hubert CHANSON ([1])

([1]) The University of Queensland, School of Civil Engineering, Brisbane QLD 4072, Australia.

([2]) University of Bordeaux, I2M, Laboratoire TREFLE, Pessac Cedex, France.

## 1. Presentation

Since there is no existing validation dataset for the sensitivity analysis on the optical flow (OF) parameters, a series of validation tests were performed in a steady plunging jet flow. A plunging jet is defined as a liquid jet impinging into a slower liquid body, with the occurrence of air entrainment, large-scale coherent structures and vortex advection (Van de Sande and Smith, 1973). The experiments were conducted in a large-scale vertical supported planar jet at the University of Queensland. The facility consisted of rectangular jet nozzle and a glass water tank. The water was supplied from a constant head tank, and was issued from the two-dimensional nozzle, discharging into a receiving pool. Figure 1 shows the experimental set-ups, previously used by Bertola et al. (2018) and Shi et al. (2018). The camera system was identical to the one in the breaking bore, including the Phantom v2011 ultra-high-speed camera, a Nikkor 50 mm f/1.4 lens and a high-intensity LED array. 23,000 frames were used to obtain time-averaged velocities by the CNL OF technique, with the frame rate of 11,303 fps. The flow conditions are summarised next to the Figure 1

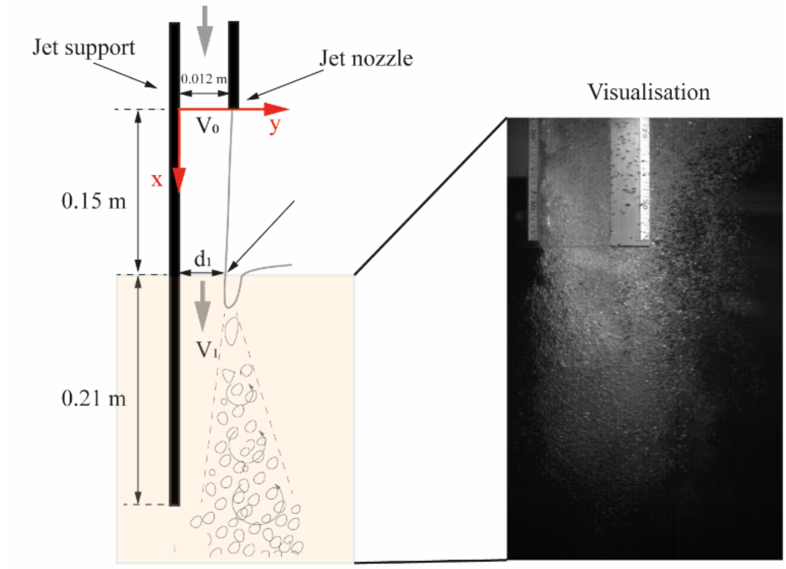


| | |
|---|---|
| $V_1$ [m/s] | 2.50 |
| $V_0$ [m/s] | 1.82 |
| $Q$ [m$^3$/s] | 0.0059 |
| $x_1$[m] | 0.15 |
| $d_1$ [m] | 0.0087 |
| *Re* | 24,511 |

$V_1$: impact velocity; $V_0$: jet nozzle velocity; $Q$: water discharge, $x_1$: jet length; $d_1$ clear-water jet thickness at impact; *Re*: Reynolds number.

Figure 1. Experimental set-up, flow visualisation and flow conditions in a steady plunging air-water jet.

## 2. Sensitivity analysis

Different OF parameters were selected, including the neighbourhood size $N$ = [5×5, 10×10, 20×20], frame rate $f_s$ = [1,000, 5,000, 11,300] and pyramid level $l_p$ = [1, 4, 7]. All the combinations of these parameters were tested, encompassing 27 test cases. Figure 2 presents the time-averaged longitudinal velocity profiles at different longitudinal locations. Note that only 8 cases are shown in Figure 2 for a better visualisation. Overall, the data showed that OF parameters significantly impacted on the velocity values. The OF profiles were compared to the air-water velocity data of Shi et al. (2018), collected under the same flow conditions. The comparison suggested two cases of suitable parameters: (1) $N$ =

5×5 pixels, $f_s$ = 11,300 fps and $l_p$ = 7; (2) $N$ = 15×15 pixels, $f_s$ = 5,000 fps and $l_p$ = 1. However, the sensitivity analysis on the number of frames showed at least 20,000 frames used to obtain a consistent velocity field, which could not be achieved with the Case 2 with 5,000 fps. Thus, Case 1 was adopted in the present study.

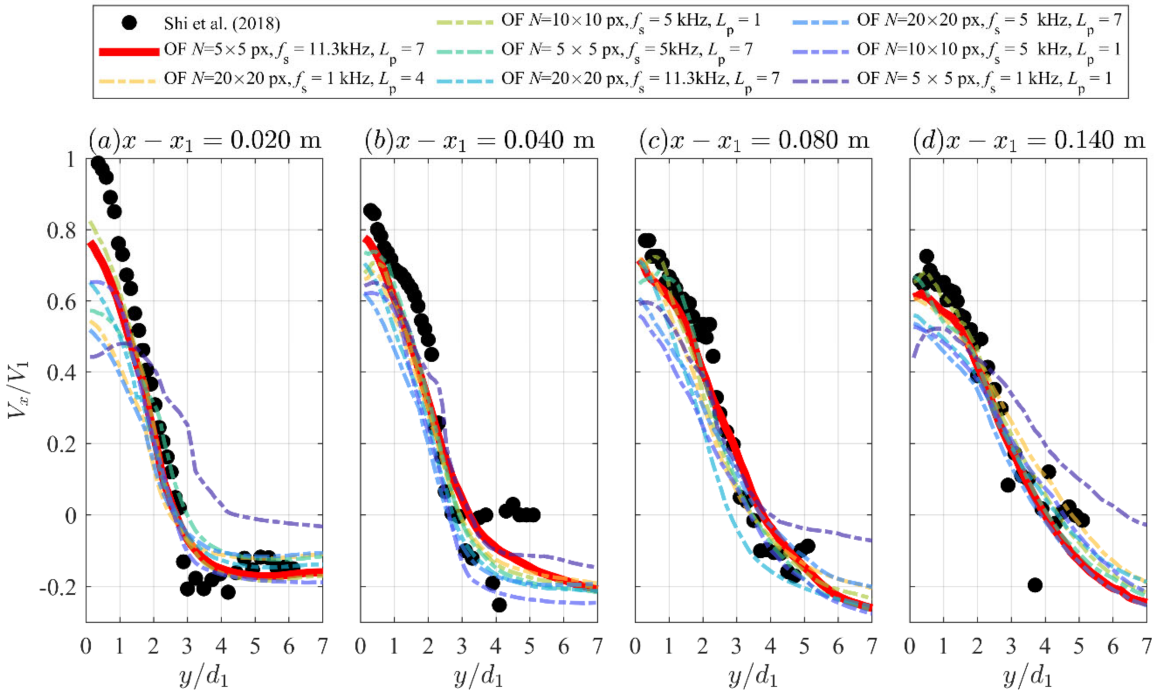


Figure 2. Sensitivity analyse of neighbourhood size $N$ (px means pixels), frame rate $f_s$ and number of pyramid levels $L_p$ - Comparison to air-water velocity data (Shi et al., 2018).

**References**

Bertola, N., Wang, H., Chanson, H., 2018. Air Bubble Entrainment, Breakup, and Interplay in Vertical Plunging Jets. J. Fluids Eng. Trans. ASME 140, 1–13. https://doi.org/10.1115/1.4039715

Shi, R., Wang, H., Chanson, H., 2018. Bubble convection and bubbly flow turbulent time and length scales in two-dimensional plunging jets. Exp. Therm. Fluid Sci. 98, 278–289. https://doi.org/10.1016/j.expthermflusci.2018.06.008

Van de Sande, E., Smith, J.M., 1973. Surface entrainment of air by high velocity water jets. Chem. Eng. Sci. 28, 1161–1168. https://doi.org/10.1016/0009-2509(73)85025-0